Univerzita Karlova v Prahe
Matematicko-fyzikálna fakulta

DIPLOMOVÁ PRÁCA

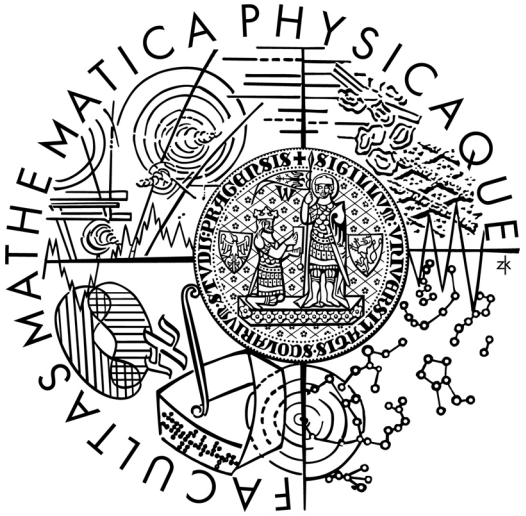

Peter Čendula

Modelovanie rastu kvantových bodiek v aproximácii elastického kontinua

Katedra fyziky kondenzovaných látek, Matematický ústav UK

Vedúci diplomovej práce:
Prof. RNDr. Václav Holý, CSc.

Štúdijný program:
Fyzika
Štúdijný obor:
Matematické a počítačové modelovanie vo fyzike a technike

Charles University Prague
Faculty of Mathematics and Physics

Master thesis

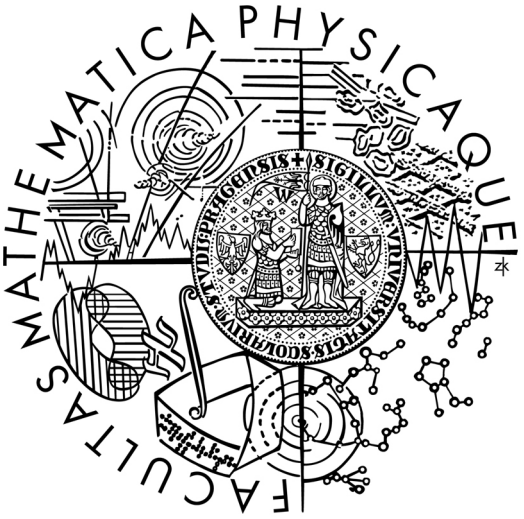

Peter Čendula

Modeling the quantum dot growth in the continuum approximation

Department of Condensed Matter Physics
Mathematical Institute of Charles University

Supervisor:
Prof. RNDr. Václav Holý, CSc.

Programme of study:
Physics
Field of study:
Mathematical and computer modeling in physics and technology

Poďakovanie

Veľmi rád by som poďakoval za pomoc, cenné rady, trpezlivosť a entuziazmus hlavne Václavovi Holému ale i ďalším - Brian Spencer, Simon Gill, Helen Eisenberg, Petr Knobloch, Zdeněk Vlášek, Milan Pokorný, Josef Málek, Yaoyu Pang. Za vytvorené podmienky ďakujem Katedre fyziky kondenzovaných látok, Nečasovmu centru pre matematické modelovanie (LC06052) a METACentru. Mojim rodičom, sestričke a Janke ďakujem za výdatnú všestrannú podporu môjho štúdia.

Čestné prehlásenie

Prehlasujem, že som svoju diplomovú prácu napísal samostatne a výhradne s použitím citovaných prameňov. Súhlasím so zapožičiavaním práce.

V Prahe, 15.12.2006

Peter Čendula

vlastnoručný podpis

Acknowledgements

I would like to thank Václav Holý for his help, valuable advices, patience and enthusiasm. Thanks also to Brian Spencer, Simon Gill, Helen Eisenberg, Petr Knobloch, Zdeněk Vlášek, Milan Pokorný, Josef Málek, Yaoyu Pang, Department of Condensed Matter Physics, Nečas Center for Mathematical Modeling (LC06052) and METACenter. To my parents, sister and Jane warm thank you for invaluable support during my studies.

Statement of Honesty

I hereby declare that I have written this master thesis separately, independently and entirely with using quoted resources. I agree that the University Library shall make it available to borrowers under rules of the Library.

Prague, 15.12.2006

Peter Čendula

Signature

Contents

Abstract

Názov práce: Modelovanie rastu kvantových bodiek v aproximácií elastického kontinua
Autor: Peter Čendula
Katedra: Katedra fyziky kondenzovaných látek, Matematický ústav UK
Vedúci diplomovej práce: Prof. RNDr. Václav Holý, CSc.
E-mail vedúceho: holy@mag.mff.cuni.cz
Abstrakt: Kvantové bodky môžu rásť spontánne počas molekulárnej epitaxie dvoch rôznych materiálov s rôznymi mriežkovými parametrami, Stranski-Krastanowov rastúci mód. Uvažujeme dvojrozmerný matematický model založený na aproximácii rastúceho filmu ako elastického kontinua. Nelineárnu evolučnú rovnicu riešime numericky pomocou metódy konečných prvkov a spektrálnymi metódami. Výpočet deformácie prevádzame do komplexných premenných a riešime pomocou tzv. Goursatovových analytických funkcií. Vplyv rozhrania film/substrát je zahrnutý v závislosti povrchového napätia na hrúbke filmu. Študujeme závislosť rastu na smerovej anizotropii povrchovej energie, stabilitu vytvorených fazetovaných bodiek a ich tvarové zmeny. Ostré rohy a silná anizotropia vedú na ťažkosti v numerickej analýze, ktorým sa dá predísť začlenením regularizačných členov. Výsledky simulácii kvalitatívne zodpovedajú experimentálnym pozorovaniam.
Kľúčové slová: kvantová tečka, anizotropie, povrchová energie, epitaxe

Title: Modeling the quantum dot growth in the continuum approximation
Author: Peter Čendula
Department: Department of Condensed Matter Physics, Mathematical Institute of Charles University
Supervisor: Prof. RNDr. Václav Holý, CSc.
Supervisor's e-mail address: holy@mag.mff.cuni.cz
Abstract: Quantum dots can grow spontaneously during molecular beam epitaxy of two materials with different lattice parameters, Stranski-Krastanow growth mode. We study a mathematical model based on the continuum approximation of the growing layer in two dimensions. Nonlinear evolution equation is solved using finite element method and spectral methods together with stress calculation based on the Goursat analytic functions. Effect of the film/substrate interface is included in the dependence of surface tension on height of the film. The effect of directional anisotropy of surface tension on the evolution is established together with stability of faceted island arrays and their shape transitions. Corner between facets and strong anisotropy lead to difficulties in the numerical analysis, which are prevented by including the regularization terms. Simulation results qualitatively agree with experiments.
Keywords: quantum dot, anisotropy, surface energy, epitaxy

Venovanie

... pre môjho ocina a maminu ;-)

Goals of the thesis

- understand heteroepitaxial growth phenomena and structural properties of quantum dots
- review the current state of continuum models for dot formation
- formulate two-dimensional growth model according to Spencer and Meiron (1994)
- perform linear stability analysis with wetting energy and anisotropic surface energy
- calculate numerically the strain energy density on the film surface and inside the film
- develop numerical methods for evolution equation
- include wetting energy to account for film/substrate interaction
- verify the ripening process for evolution of large samples
- inspect the consequences of material deposition
- include corner regularization in order to follow the evolution after creation of corners between facets
- study the effect of anisotropic surface energy on the evolution of faceted islands
- examine if the cusped surface energy enhances the stability of island arrays
- study the shape transitions of growing islands
- find major factors influencing island final morphology and stability
- compare simulation results with experimental observations

Introduction

Quantum dots were first developed in 1970s and ever since they attracted huge research interest among physicists, chemists and biologists. Many ways of production were developed (colloidal synthesis, electron beam lithography, epitaxy) and here we will only focus on the bottom-up self-organizing process in heteroepitaxy (island growth, Stranski-Krastanow growth) promising to produce regular quantum dot arrays for quantum cryptography and quantum computers.

Roughening and growth of undulated strained solid films was long seen as a degradation mechanism during planar film growth. It has been realized around 1990 that this could be a way to fabricate quantum nanostructures. It is well understood that islands form through stress-driven morphological instability (ATG-instability, 1972) to reduce the total elastic strain energy in the system. Many gaps in theory and experiment have been filled in recent years, but the production of commercial island arrays is still not possible.

Number of works studied continuum approach to the growth problem. Stress-driven instability in a semi-infinite solid was studied by Spencer and Meiron (1994), Yang and Srolovitz (1993) and it leads to the formation of cusps. This is prevented in heteroepitaxy by strong film/substrate interaction, since the film wets the substrate and Chiu and Gao (1995), Kukta and Freund (1997), Spencer (1999) studied the free boundary problem to determine the equilibrium island shape for isotropic surface energy. Either boundary layer model or height-dependent surface energy was used to smooth the abrupt change in material properties at the film/substrate interface. Zero contact angle of island edges to the film wetting the substrate was derived for isotropic case. Long-time annealing of isotropic films reveals growth of larger islands at the expense of smaller, so called ripening (coarsening), which is undesirable effect for fabrication. These works did not give physical explanation of experimentally observed island facets and initial growth stages.

Equilibrium study by Tersoff et al. (2002) first explained the prepyramid to pyramid shape transition with the assumption of anisotropic surface energy. Dynamical studies were carried out in 2D with smooth and cusped surface energy by Long et al. (2001); Eisenberg and Kandel (2005) with special numerical approaches. They both concluded that the evolution timeline is best explained with the assumption of cusped surface energy below roughening temperature and the latter found stable island array against ripening, consistent with observations of Medeiros-Ribeiro et al. (1998).

Strength of the surface anisotropy is critical for the evolution problem, as for strong anisotropy the evolution problem can become ill-posed, with the leading negative fourth derivative. In this case corner energy regularization can be introduced, but it was considered dynamically only by Siegel et al. (2004) for evolution of voids in elastic solid and not in the context of quantum dot growth.

This work aims to cover only the basic properties of quantum dot formation, evolution and stability from the continuum simulations. Main results of our work are: successful numerical treatment of the evolution equation including the strong anisotropic surface energy and island edges, calculations of ripening process, development of faceted islands for anisotropic surface energy and their metastability against ripening for cusped surface energy. Experimental characteristics of growth, including island growth only above critical wetting layer thickness, constant aspect ratio of growing faceted islands, shape transitions and stability were qualitatively reproduced.

Chapter 1

Quantum dots

1.1 Properties and applications

Quantum dot(QD) is a tiny semiconductor crystal with size in the order of nanometers, hence the names "dot" or "island", Figure 1.1. It is also often called "artificial atom" because of its quantum properties, but it actually contains roughly hundreds to thousands real atoms.

In the bulk semiconductor material(several times bigger than 10 nm), charge carriers can have a range of energies. These energies are so close together, that they can be described as continuous. There is certain forbidden range of energies called bandgap. Almost all carriers naturally occupy the energy levels below the bandgap (valence band) and only very few of them are in the conduction band (above the bandgap). They can jump to the conduction band when they get additional energy from outside (heat, radiation) and they leave a "hole" in the valence band. This electron-hole pair is called an exciton and there is an average distance between them called Exciton Bohr Radius. If the size of the semiconductor is comparable with this value, the energy spectrum is no longer continuous and has to be treated as discrete. Carriers are thus confined inside the dot, similarly to an atom. So the quantum dot is actually a three dimensional quantum well known from the basic quantum mechanics. The width of the quantum dot bandgap depends on its size and chemical composition, making it easy to tune absorption and emission spectra, what is impossible for atoms, but desirable for optical properties.

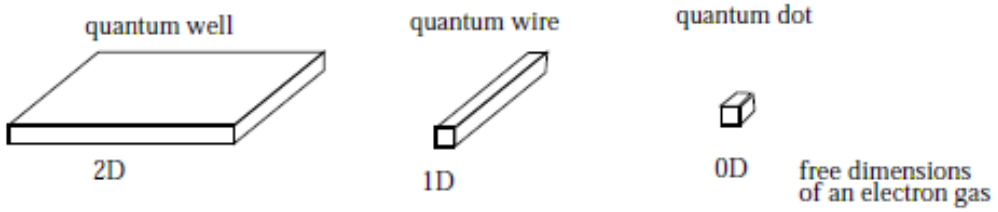

Figure 1.1: Schematic figure of various nanostructures.

Because they are so small, they have very sharp density of states and thus superb transport and optical properties for detectors, lasers and amplifiers. Quantum dots have also large quantum yield, the percentage of absorbed photons that result in emitted photons, what is being studied for potential use in more effective solar cells.

There are already working quantum dots around us to date. New generation of Blue-ray disc and Playstation 3 uses QD based blue-violet laser with smaller wavelength than traditional HeNe lasers and is able to read more dense data. Organic dyes with quantum dots have better brightness and stability. Organized arrays of quantum dots could serve as quantum chips for performing quantum operations.

1.2 Self-organized growth

When one material is being deposited on another (with different lattice constant) during molecular beam epitaxy (MBE), the growing layer laterally fits the crystal lattice of the substrate and is therefore elastically deformed. It is known, that such a stressed film is unstable (Asaro-Tiller-Grinfeld (ATG) instability) against perturbations with wavelength greater than (Srolovitz (1989); Stangl et al. (2004))

$$\lambda_{crit} = \frac{\pi\tilde{\gamma}}{\varepsilon_0^2 E(1-\nu^2)}, \tag{1.1}$$

where ν is Poisson's ratio of the film, E its Young's modulus, $\tilde{\gamma}$ isotropic surface energy (per unit area) and ε_0 is the misfit strain of the growing layer with respect to the substrate. The fastest growing perturbation has wavelength $\frac{4\lambda_{crit}}{3}$ and determines the periodicity of the final morphology.

There are three scenario of heteroepitaxy (Figure 1.2), continuous layer-by-layer Frank-van der Merwe mode, island formation without wetting layer in between during Volmer-Weber mode and Stranski-Krastanow growth mode when layer-by-layer growth is observed usually up to a critical thickness of few monolayers (ML) Mo et al. (1990), when a 3D island morphology is energetically more favorable, Figure 1.3. The onset of the ATG instability in the initial growth stages is suppressed by the wetting effect at the film/substrate interface Chiu and Gao (1995); Spencer (1999); Tekalign and Spencer (2004) or due to the elastic anisotropy in the growing layer Eisenberg and Kandel (2002). This clustering from flat film into 3D islands at preferable wavelength is the core of the self-organizing process.

Generally, elastic energy stored in the growing layer competes with its surface energy and provides possibility for nonplanar morphologies.

1.3 Observed properties

We have used extensive review on structural properties of quantum nanostructures by Stangl et al. (2004). Germanium islands on Si were first observed

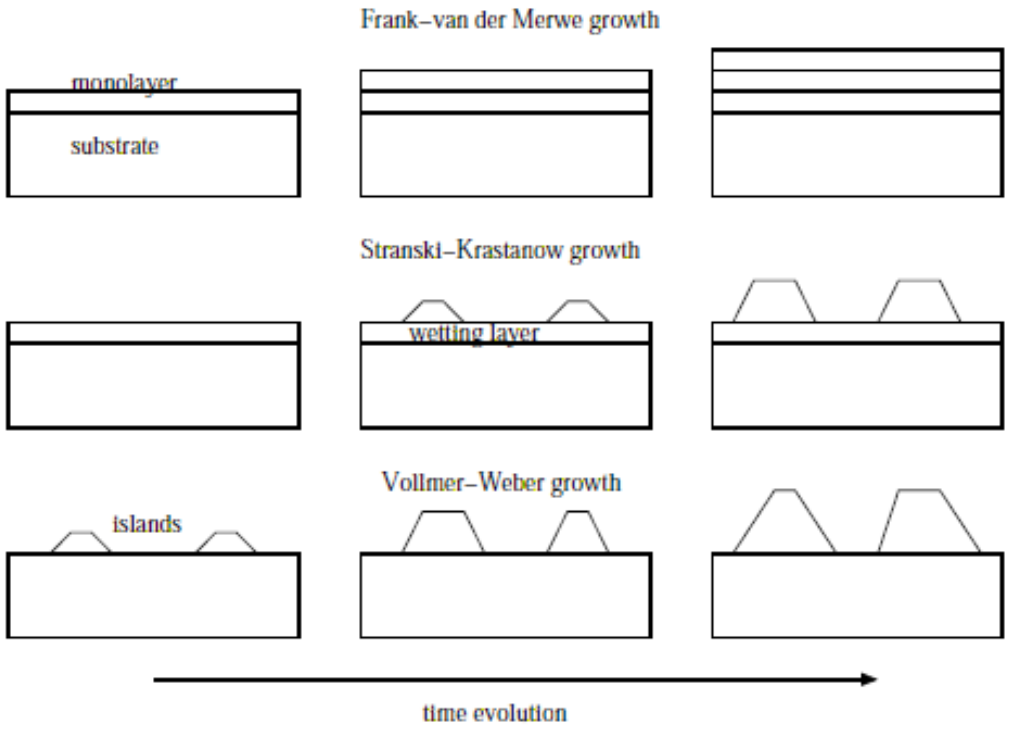

Figure 1.2: Various modes of the heteroepitaxial growth.

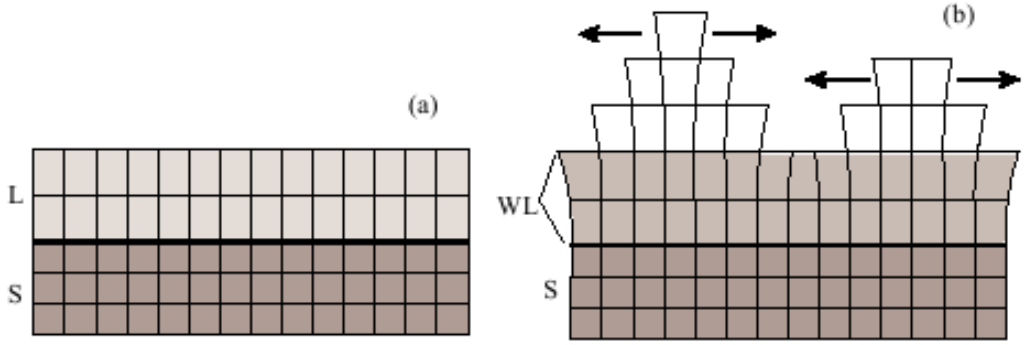

Figure 1.3: In the first stage of the Stranski-Krastanow growth mode, pseudomorphic layer is grown (a). After the layer thickness exceeds critical value island morphology is created (b). Wetting layer is denoted WL, growing layer L and substrate S.

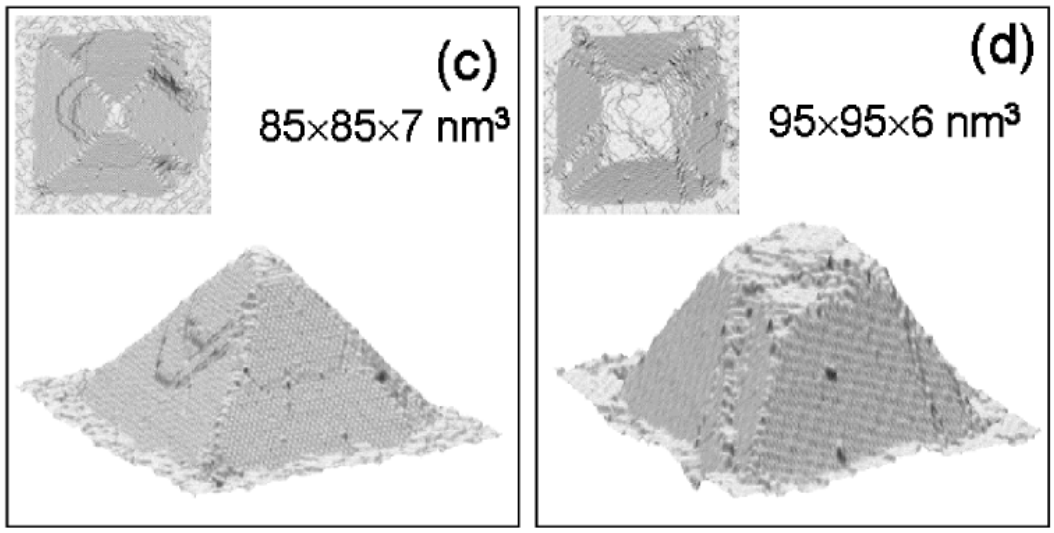

Figure 1.4: Typical Ge pyramid islands obtained by STM during Si capping (left 2 ML, right 4 ML) of Ge domes grown on Si(001) Rastelli et al. (2001). Beautiful facets {105} have angle 11°.

by Mo et al. (1990) as square base pyramids with (105) facets (11°), Figure 1.4. SiGe islands are additionally observed as prepyramids (shallow mounds), hut clusters (elongated pyramids with (105) facets) and multifaceted domes (with facets (105),(113), (15 3 23)), Figures 1.5. The pyramid-to-dome shape transition during growth was experimentally observed by Kamins et al. (1997); Medeiros-Ribeiro et al. (1998); Ross et al. (1998) and numerically calculated in the work of Eisenberg and Kandel (2005). Even bigger islands called "superdomes" can be grown, but dislocations appear at their base as strain is more effectively relieved above some critical size. They will be not considered in this work.

Postgrowth annealing studies have shown that pyramids and domes are stable against ripening in some temperature range, caused by the stronger surface energy anisotropy relative to the strain relaxation. At higher temperatures surface energy is more isotropic and ripening was observed. Island size distribution evolves from prepyramids to pyramids and then to domes with increasing diameter, Figure 1.6.

Lateral interaction of quantum dots at the same surface weakly influences the size distribution and periodicity of island positions. Island multilayers show influence of island position on the surface from elastic interaction of the buried island layers, which can result in vertically or oblique aligned islands in the superlattice, depending on the elastic anisotropy of the material.

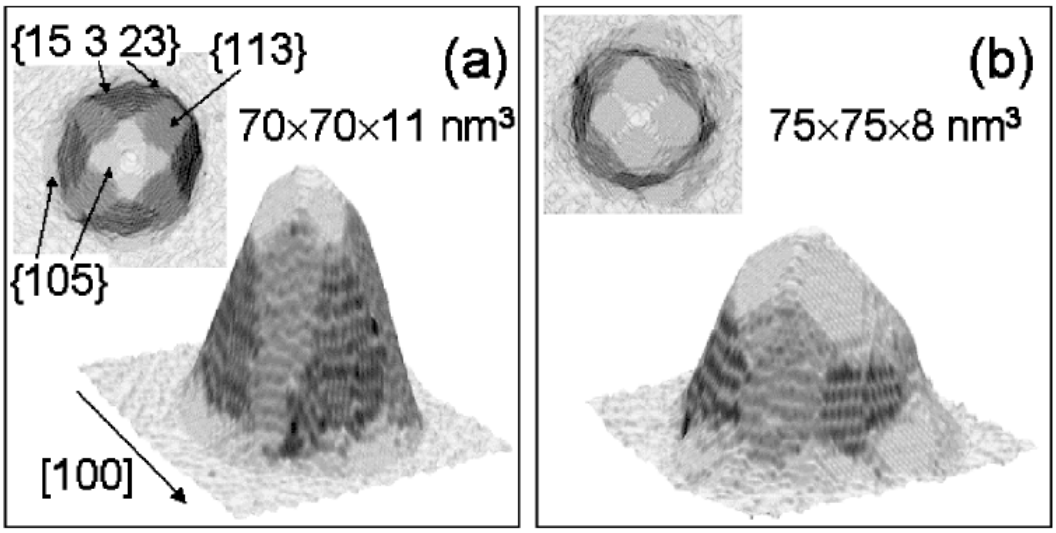

Figure 1.5: Typical Ge dome islands obtained by STM during Si capping (left uncapped, right 1 ML) of Ge domes grown on Si(001) Rastelli et al. (2001). Facets are denoted in the inset picture.

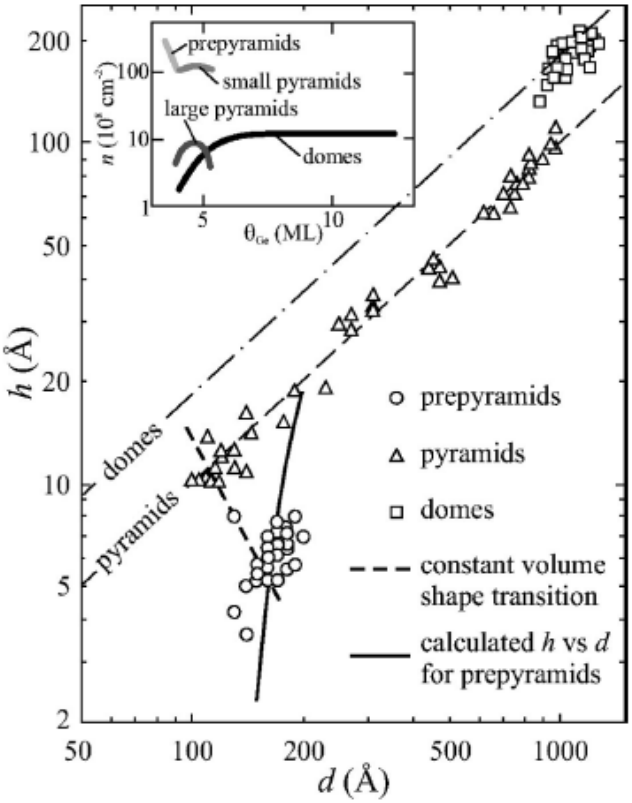

Figure 1.6: Island height h as a function of island diameter d during deposition of Ge on Si(001). The inset shows the time evolution of the island density for different island types, from Stangl et al. (2004).

Chapter 2

Continuum model of thin film growth

We will describe the continuum approximation of thin strained film (dislocation free) in 2D. Evolution equation with wetting energy and corner regularization is derived in nondimensional form. Goursat analytic functions are used to formulate the elastic problem as boundary integral equation. Different surface energy anisotropies are introduced, isotropic, smooth and cusped. Linear stability analysis is performed with anisotropic surface energy. Illustration of material parameters and characteristic quantities for Ge/Si and InAs/GaAs follows.

2.1 Strained epitaxial film

Our model would like to describe the evolution of faceted quantum dots during the thin film growth with the wetting effect. We will follow Spencer and Meiron (1994); Tekalign and Spencer (2004) in model formulation, but we will assume anisotropic surface energy.

Let us simplify the problem to two dimensions, assuming only plane cut perpendicular to the film surface. This is often denoted as $1+1$ system of 2D film with 1D surface. Some important features of the film evolution can be studied in this case. Our model is equivalent to the equally elongated film and substrate in the third dimension, with no strain in the third dimension (plane strain is assumed). Strained film in this 2D model is a region between the graph of a function $Y = H(X,T)$ and $Y = 0$ in Cartesian coordinates X, Y, see Figure 2.1. The film is allowed to evolve in time T. Substrate occupies the region under $Y = 0$.

Material is deposited from above the film with constant deposition rate V_D either normal to the X axis (MBE), what results in vertical deposition rate

$$J_D(X,T) = V_D \tag{2.1}$$

or normal to the film surface (liquid phase epitaxy, LPE), what yields

$$J_D(X,T) = V_D\sqrt{1+H_X^2}. \tag{2.2}$$

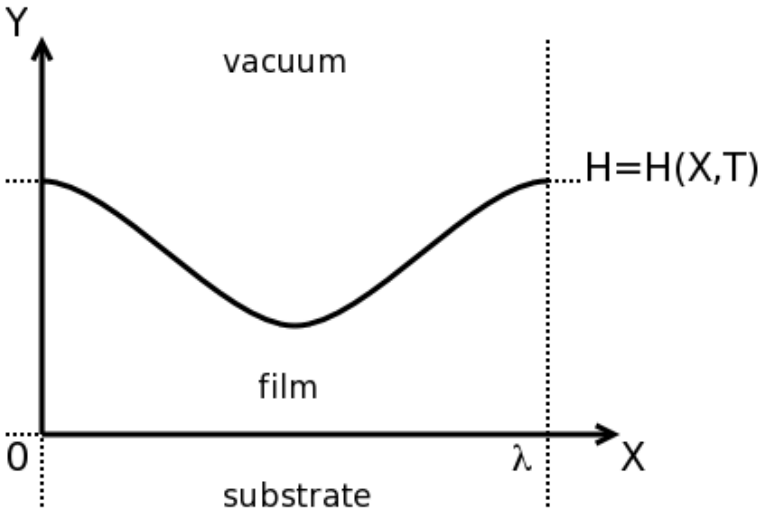

Figure 2.1: Strained epitaxial film.

The region above the film is otherwise ultrahigh-vacuum.

System is supposed to occupy the domain $\langle 0, \Lambda \rangle \times \mathbb{R}$ and repeat itself periodically in the X axis.

We choose the reference state of a uniform undeformed substrate crystal lattice for the measurement of strains. Relative difference between lattice constants of the substrate a_s and the film a_f is the so-called "mismatch strain"

$$\varepsilon_0 = \frac{a_s - a_f}{a_f} \tag{2.3}$$

and it is usually negative (compression), as $a_f > a_s$. During the film deposition, its crystal lattice is deformed to fit the crystal lattice of the substrate. Both the film and the substrate are supposed to be isotropic linear elastic materials with the same elastic constants (what is reasonable e.g. for Ge/Si and InAs/GaAs systems) and obey usual Hooke's law

$$\varepsilon_{ij} = \frac{1+\nu}{E}\tilde{\sigma}_{ij} - \frac{\nu}{E}\tilde{\sigma}_{kk}\delta_{ij}, \tag{2.4}$$

where ε_{ij}, E, ν are strain tensor, Young modulus and Poisson's ratio. Their response to strains is thus identical and it is useful to view the problem as a stressed semi-infinite film under the interface $Y = H(X,T)$ subject to the condition of mechanical equilibrium for the stress tensor $\tilde{\sigma}_{ij}$ (indices represent coordinates X, Y)

$$\partial_j \tilde{\sigma}_{ij} = 0 \qquad \text{in} \qquad Y < H(X,T) \tag{2.5}$$

and boundary condition without normal forces to the surface (traction-free interface)

$$\tilde{\sigma}_{ij} N_j = 0 \qquad \text{on} \qquad Y = H(X,T), \tag{2.6}$$

where $N_j = (N_X, N_Y)$ is the unit outer normal. This simplified view is valid until $H(X,T) > 0$, what will be guaranteed by the wetting effect implicitly.

There should be only the uniaxial stress far away under the interface $H(X,T)$,

$$\tilde{\sigma}_{ij} = \begin{pmatrix} \sigma_0 & 0 \\ 0 & 0 \end{pmatrix} \qquad \text{for} \qquad Y \to -\infty, \tag{2.7}$$

where $\sigma_0 = \frac{E\varepsilon_0}{1-\nu^2}$ is the "mismatch stress" for the case of a flat film. The stresses in the film are then given by $\tilde{\sigma}_{ij}$ and in the substrate by

$$\tilde{\sigma}_{ij} - \begin{pmatrix} \sigma_0 & 0 \\ 0 & 0 \end{pmatrix}, \tag{2.8}$$

since the substrate has different lattice parameter and there are no stresses far away under the interface film/substrate. We need to calculate the strain energy density $\tilde{S}$ at the surface of the film, which affects the mass transport on the surface. It is given by

$$\tilde{S} = \frac{1}{2}\varepsilon_{ij}\tilde{\sigma}_{ij}. \tag{2.9}$$

Since we assumed the plane strain conditions, we can write

$$\varepsilon_{ij} = \begin{pmatrix} \varepsilon_{XX} & \varepsilon_{XY} & 0 \\ \varepsilon_{XY} & \varepsilon_{YY} & 0 \\ 0 & 0 & 0 \end{pmatrix}, \tag{2.10}$$

where the Z axis is assumed in the perpendicular direction to the XY plane. According to Hooke's law (2.4), the mixed components of stress with Z index have to be zero

$$0 = \varepsilon_{XZ} = \frac{1+\nu}{E}\tilde{\sigma}_{XZ} \qquad \Rightarrow \qquad \tilde{\sigma}_{XZ} = 0, \tag{2.11}$$

$$0 = \varepsilon_{YZ} = \frac{1+\nu}{E}\tilde{\sigma}_{YZ} \qquad \Rightarrow \qquad \tilde{\sigma}_{YZ} = 0, \tag{2.12}$$

and other nontrivial relations hold

$$\varepsilon_{XX} = \frac{1+\nu}{E}\tilde{\sigma}_{XX} - \frac{\nu}{E}(\tilde{\sigma}_{XX} + \tilde{\sigma}_{YY} + \tilde{\sigma}_{ZZ}), \tag{2.13}$$

$$\varepsilon_{XY} = \frac{1+\nu}{E}\tilde{\sigma}_{XY}, \tag{2.14}$$

$$\varepsilon_{YY} = \frac{1+\nu}{E}\tilde{\sigma}_{YY} - \frac{\nu}{E}(\tilde{\sigma}_{XX} + \tilde{\sigma}_{YY} + \tilde{\sigma}_{ZZ}), \tag{2.15}$$

$$\varepsilon_{ZZ} = 0 = \frac{1+\nu}{E}\tilde{\sigma}_{ZZ} - \frac{\nu}{E}(\tilde{\sigma}_{XX} + \tilde{\sigma}_{YY} + \tilde{\sigma}_{ZZ}). \tag{2.16}$$

From the last equation we have

$$\tilde{\sigma}_{ZZ} = \nu(\tilde{\sigma}_{XX} + \tilde{\sigma}_{YY}), \tag{2.17}$$

and thus the stress tensor looks like

$$\tilde{\sigma}_{ij} = \begin{pmatrix} \tilde{\sigma}_{XX} & \tilde{\sigma}_{XY} & 0 \\ \tilde{\sigma}_{XY} & \tilde{\sigma}_{YY} & 0 \\ 0 & 0 & \nu(\tilde{\sigma}_{XX} + \tilde{\sigma}_{YY}) \end{pmatrix}. \tag{2.18}$$

Then, the strain energy density (2.9)

$$\tilde{S} = \frac{1}{2}(\varepsilon_{XX}\tilde{\sigma}_{XX} + 2\varepsilon_{XY}\tilde{\sigma}_{XY} + \varepsilon_{YY}\tilde{\sigma}_{YY}), \tag{2.19}$$

$$\tilde{S} = \frac{1+\nu}{2E}\left(\tilde{\sigma}_{XX}^2 + \tilde{\sigma}_{YY}^2 - \nu(\tilde{\sigma}_{XX} + \tilde{\sigma}_{YY})^2 + 2\tilde{\sigma}_{XY}^2\right), \tag{2.20}$$

and on the interface of the film with the use of boundary condition (2.6)

$$\tilde{S} = \frac{1-\nu^2}{2E}(\tilde{\sigma}_{XX} + \tilde{\sigma}_{YY})^2. \tag{2.21}$$

Nonlinearity in the boundary condition implies we have to solve for stresses numerically in general, what will be done by introducing Goursat analytic functions and solving equivalent boundary integral equation for them (see Section 2.6). Strain energy density will be plugged into the evolution equation as the driving force.

2.2 Evolution equation

Interface of the film can move by mass transport under the influence of chemical potential. We assume that surface diffusion is the dominant transport mechanism. We neglect evaporation and volume diffusion but we allow condensation of deposited atoms. In our view, all impinging atoms stick on the interface and then diffuse by surface diffusion. The net change in the number of atoms along the surface causes it to move normal to itself with velocity

$$V_n = J_D N_Y - \nabla_S J_S, \tag{2.22}$$

where $N_Y = \frac{1}{\sqrt{1+H_X^2}}$ and ∇_S is the surface gradient operator

$$\nabla_S = \frac{1}{\sqrt{1+H_X^2}}\frac{\partial}{\partial X}, \tag{2.23}$$

$$H_X = \frac{\partial H}{\partial X}. \tag{2.24}$$

Atoms tend to move from places with higher chemical potential to places with smaller chemical potential, also the surface diffusion flux J_S is proportional to the negative gradient of the chemical potential at the surface $\tilde{\mu}$

$$J_S = -\frac{\nu_S D_S V_{at}}{k_B \Theta}\nabla_S \tilde{\mu}, \tag{2.25}$$

where V_{at} is the atomic volume of the film, ν_S is the number of atoms per unit area of the surface, D_S is the surface diffusivity, k_B Boltzmann constant and Θ is the absolute temperature. The chemical potential on the surface $\tilde{\mu}$ consist from the surface energy term $\tilde{\mu}_{surf}$, strain energy term $\tilde{\mu}_{el}$, wetting energy term $\tilde{\mu}_{wet}$ and corner energy contribution $\tilde{\mu}_{cor}$

$$\tilde{\mu} = V_{at}(\tilde{\mu}_{surf} + \tilde{\mu}_{el} + \tilde{\mu}_{wet} + \tilde{\mu}_{cor}). \tag{2.26}$$

We denote surface free energy (per unit area) with $\tilde{\gamma}$. For most crystals, it depends on the orientation angle θ, defined as the angle between unit outward surface normal $\mathbf{n}$ to the X axis. Its contribution to the chemical potential on the interface can be obtained by minimizing $\int \tilde{\gamma}(\theta) ds$ over the volume preserving variations of the interface Eisenberg and Kandel (2002); Siegel et al. (2004), what implies the equation

$$\tilde{\mu}_{surf} = (\tilde{\gamma} + \frac{\partial^2 \tilde{\gamma}}{\partial \theta^2}) K, \tag{2.27}$$

$$\tilde{\Upsilon} = \tilde{\gamma} + \frac{\partial^2 \tilde{\gamma}}{\partial \theta^2}, \tag{2.28}$$

$$K = -\frac{\partial}{\partial X} \left(\frac{H_X}{\sqrt{1 + H_X^2}} \right), \tag{2.29}$$

where $\tilde{\Upsilon}$ denotes "surface stiffness" and K mean curvature. Elastic energy contribution is simply

$$\tilde{\mu}_{el} = \tilde{S}. \tag{2.30}$$

Finally

$$\tilde{\mu} = V_{at}(\tilde{\Upsilon} K + \tilde{S} + \tilde{\mu}_{wet} + \tilde{\mu}_{cor}). \tag{2.31}$$

Because the interface moves normal to itself, it has greater velocity in vertical Y axis

$$\frac{\partial H}{\partial T} = V_n \sqrt{1 + H_X^2} \tag{2.32}$$

and the evolution equation (2.22) is then

$$\frac{\partial H}{\partial T} = J_D + D \frac{\partial}{\partial X} \left[\frac{1}{\sqrt{1 + H_X^2}} \frac{\partial}{\partial X} \left(\tilde{\Upsilon} K + \tilde{S} + \tilde{\mu}_{wet} + \tilde{\mu}_{cor} \right) \right], \tag{2.33}$$

with constant $D = \frac{\nu_S D_S V_{at}^2}{k_B \Theta}$. Generally, surface energy stabilizes the interface and the elastic energy is responsible for the destabilization. Ratio of these two affects the evolution of the film. The nonlinear character of the problem cannot be simplified by linearization, since the slopes of faceted quantum dots $(11°, 45°)$ exceed small angles.

We require periodic boundary values of all functions, especially

$$H(0, T) = H(\Lambda, T). \tag{2.34}$$

The first derivatives should be also periodic at the boundary (for the weak formulation)

$$\frac{\partial H(0, T)}{\partial X} = \frac{\partial H(\Lambda, T)}{\partial X}. \tag{2.35}$$

Last assumption is the periodic surface flux of atoms at the boundary

$$J_S(0, T) = J_S(\Lambda, T). \tag{2.36}$$

This condition can be written using previous equations for chemical potential

$$\frac{\partial\tilde{\mu}}{\partial X}(0,T) = \frac{\partial\tilde{\mu}}{\partial X}(\Lambda,T). \tag{2.37}$$

Small sinusoidal perturbation of amplitude P_0 of the flat film surface of height H_f with fastest growing wavenumber A are assumed

$$H(X,0) = H_0(X) = H_f + P_0\cos(AX). \tag{2.38}$$

Other simulations start with random small amplitude (typically 10^{-5}) perturbation of the flat film on a bigger interval.

When the initial condition is even, the solution $H(X,T)$ at later times must be also even (governing equations are symmetric with respect to $-X$). Because of the periodicity, they must be also even around $\frac{\Lambda}{2}$ and we can handle all variables only in the first half of the interval explicitly. If the initial condition is random we compute the variables independently in whole interval.

2.3 Wetting energy

Surface energy of the film $\tilde{\gamma}_f$ is typically smaller than the surface energy of the substrate $\tilde{\gamma}_s$ and therefore the film tends to cover the substrate (than it has smaller total surface energy). At the film/substrate interface, there is an abrupt change between surface energy of the film and the substrate, which we smooth by height dependent surface energy from Tekalign and Spencer (2004) based on the transition thickness parameter B

$$\tilde{\gamma}(H) = \frac{1}{2}(\tilde{\gamma}_f + \tilde{\gamma}_s) + \frac{1}{\pi}(\tilde{\gamma}_f - \tilde{\gamma}_s)\arctan\left(\frac{H}{B}\right), \tag{2.39}$$

which can be seen on Figure 2.2. It was shown by Spencer (1999), that the results are independent of the transition function chosen in the limit of vanishing boundary layer thickness.

We obtain the wetting energy term by minimization of total surface free energy

$$\int \tilde{\gamma}(H)\sqrt{1+H_X^2}\mathrm{d}X \tag{2.40}$$

with constraint of constant area

$$\int H\mathrm{d}X = \text{const.} \tag{2.41}$$

This leads to the Euler-Lagrange equation for

$$Q = \tilde{\gamma}(H)\sqrt{1+H_X^2} - \tilde{\mu}H, \tag{2.42}$$

$$0 = \frac{\partial Q}{\partial H} - \frac{\mathrm{d}}{\mathrm{d}X}\frac{\partial Q}{\partial H_X}, \tag{2.43}$$

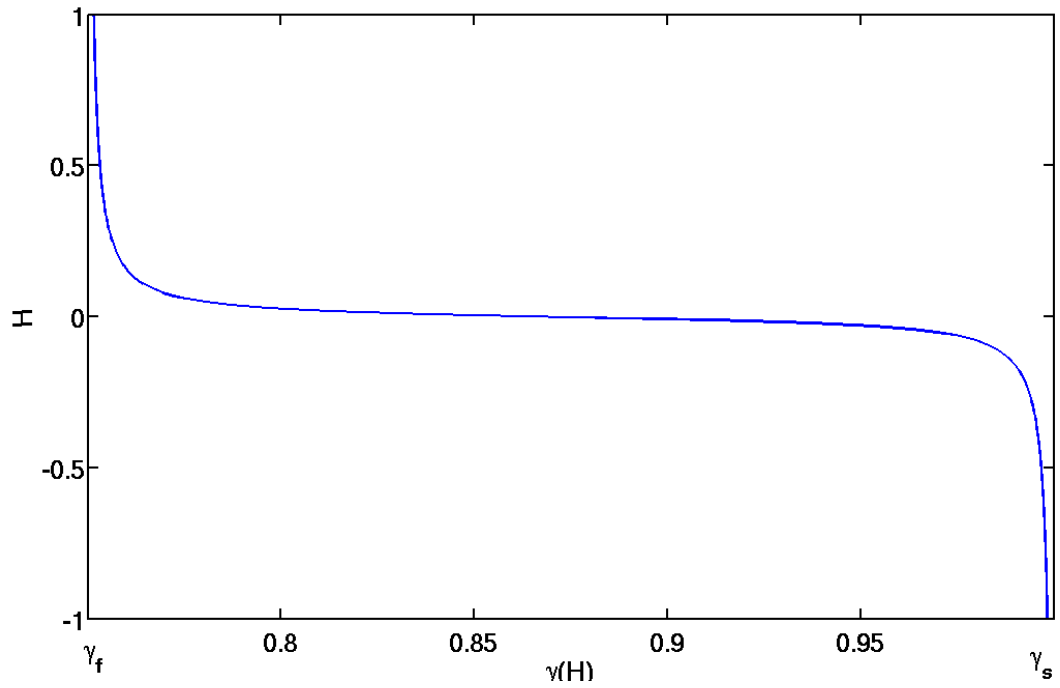

Figure 2.2: Transition in the surface energy over the film thickness for $B = 0.02$.

where we have identified the Lagrange multiplier $\tilde{\mu}$ with chemical potential. With

$$\frac{\partial Q}{\partial H} = \tilde{\gamma}'(H)\sqrt{1+H_X^2} - \tilde{\mu}, \tag{2.44}$$

$$\frac{\partial Q}{\partial H_X} = \frac{\tilde{\gamma}(H)H_X}{\sqrt{1+H_X^2}}, \tag{2.45}$$

we end up

$$\tilde{\mu} = \tilde{\gamma}(H)K + \tilde{\gamma}'(H)N_Y. \tag{2.46}$$

First term is the chemical potential from the surface energy and second from the wetting interaction. Thus

$$\tilde{\mu}_{wet} = N_Y\tilde{\gamma}'(H) = \frac{\tilde{\gamma}_f - \tilde{\gamma}_s}{\pi\sqrt{1+H_X^2}}\frac{B}{B^2+H^2}. \tag{2.47}$$

2.4 Corner energy regularization

In case of anisotropic surface energy, the surface can rapidly develop apparent corners at the edges between different facets. On the other hand, evolution problem may be ill-posed when the surface stiffness becomes negative. This leads to divergent numerical behavior, which can be prevented by including the higher-order regularization term Tersoff et al. (2002); Siegel et al. (2004) to the

surface energy, which rounds the corners slightly and stabilizes the numerical scheme

$$\tilde{\gamma}_R = \tilde{\gamma}(\theta) + \frac{R}{2}K^2. \tag{2.48}$$

Corners have large curvature and make the regularized surface energy diverge. It is physically well-founded and it contains the energy of atomic steps on the crystal surface and their interaction. Chemical potential term is then derived minimizing the free energy functional as in previous section and leads to

$$\tilde{\mu}_{cor} = -R\left(\frac{K^3}{2} + \frac{\mathrm{d}^2 K}{\mathrm{d}s^2}\right), \tag{2.49}$$

where s is arclength. It has almost no effect in the regions outside edges, since there the curvature is small. Regularization parameter R is typically very small and the simulation results should be not affected by its value if it is sufficiently small. It depends on the real miscut of the surfaces. Regularization term is inherently stiff, since it contains power and second derivative of curvature. It has to be treated implicitly in numerics therefore.

It was shown by Spencer (2004) that when the stress is absent, corner solutions of the Wulff shape can be obtained by including the regularization and the limit of $R \to 0$. In the presence of stress, only one work Siegel et al. (2004) dealt with the effect of regularization and it concluded that different corner angles are probably obtained.

2.5 Nondimensional governing equations

It is useful to formulate the equations for nondimensional variables. Characteristic values (in physical units) for different quantities are denoted with subscript 0

$$\tilde{\gamma} = \gamma_0 \gamma, \tag{2.50}$$

$$\tilde{S} = S_0 S, \quad S_0 = \frac{E\varepsilon_0^2}{2(1-\nu^2)}, \tag{2.51}$$

$$S = (1 + \sigma_{xx} + \sigma_{yy})^2, \tag{2.52}$$

Characteristic length l_0 and time τ_0 quantify the scale at which surface energy and elastic energy are fairly equal

$$l_0 = \frac{\gamma_0}{S_0}, \quad \tau_0 = \frac{\gamma_0^3}{DS_0^4}. \tag{2.53}$$

We introduce nondimensional variables $x, y, t, h(x,t), \kappa, \mu_{wet}, \mu_{cor}, j_d$ with appropriate scalings to dimensional variables $X, Y, T, H(X,T), K, \tilde{\mu}_{wet}, \tilde{\mu}_{cor}, J_D$

$$X = xl_0, \quad Y = yl_0, \quad T = t\tau_0, \quad H = hl_0, \tag{2.54}$$

$$K = \frac{\kappa}{l_0}, \quad \tilde{\mu}_{wet} = \frac{\gamma_0}{l_0}\mu_{wet}, \quad J_D = \frac{l_0}{\tau_0} j_d, \tag{2.55}$$

$$\mu = \Upsilon\kappa + S + \mu_{wet} + \mu_{cor} \tag{2.56}$$

Other nondimensional variables are denoted also as small letters or without tilde. The stress tensor is obtained with

$$\tilde{\sigma}_{ij} = \sigma_0 \left[\begin{pmatrix} 1 & 0 \\ 0 & 0 \end{pmatrix} + \sigma_{ij} \right] \tag{2.57}$$

Let us define the interval $\Omega = \langle 0, \lambda \rangle$ and its boundary $\partial\Omega = \{0, \lambda\}$. The wavelength of the solution is denoted λ and the wavenumber $a = \frac{2\pi}{\lambda}$.

We are looking for the stress tensor (to compute the strain energy density) which satisfies (2.5), (2.6), (2.7)

$$\begin{aligned} \partial_j \sigma_{ij} &= 0 \quad \text{in} \quad y < h(x,t), \\ n_j \sigma_{ij} &= f_i \quad \text{on} \quad y = h(x,t), \\ \sigma_{ij} &\to 0 \quad \text{as} \quad y \to -\infty, \end{aligned} \tag{2.58}$$

$\forall x \in \mathbb{R}$, $t \geq 0$ fixed and $f_i = (-n_x, 0)$.

We want to find two functions $h(x,t), \kappa(x,t) : \Omega \times \langle 0, T \rangle \to \mathbb{R}$, even around $\frac{\lambda}{2}$, such that

$$\kappa = -\frac{\partial}{\partial x} \left(\frac{h_x}{\sqrt{1 + h_x^2}} \right) \quad \text{in} \quad \Omega \times \langle 0, T \rangle, \tag{2.59}$$

$$\frac{\partial h}{\partial t} = j_d + \frac{\partial}{\partial x} \left[\frac{1}{\sqrt{1 + h_x^2}} \frac{\partial \mu}{\partial x} \right] \quad \text{in} \quad \Omega \times \langle 0, T \rangle, \tag{2.60}$$

(now T denotes end of the nondimensional time interval) satisfying boundary conditions (2.34), (2.35), (2.37) on $\partial\Omega \times \langle 0, T \rangle$

$$h(0,t) = h(\lambda, t), \tag{2.61}$$

$$\frac{\partial h}{\partial x}(0,t) = \frac{\partial h}{\partial x}(\lambda, t), \tag{2.62}$$

$$\frac{\partial \mu}{\partial x}(0,t) = \frac{\partial \mu}{\partial x}(\lambda, t), \tag{2.63}$$

Initial conditions used are

$$h(x,0) = h_0(x) = h_f + p_0 \cos(ax) \tag{2.64}$$

or random small p_0 amplitude perturbation of the flat film.

2.6 Strain energy calculation

Because of the two dimensional geometry, we can solve the elasticity equations using transformation to complex Goursat functions φ, ψ analytic in the domain of the semi-infinite film (denoted Π) as in Spencer and Meiron (1994). We will briefly present the derivation of the resulting nonsingular integral equation Mikhlin (1957). It will be then solved by numerical quadrature in the Section 3.1.

Let $z = x + iy$, then stresses and displacements are determined with

$$\begin{aligned} \sigma_{xx} + \sigma_{yy} &= 4\mathrm{Re}[\varphi'(z)], \\ -\sigma_{xx} + \sigma_{yy} + 2i\sigma_{xy} &= 2[\bar{z}\varphi''(z) + \psi'(z)], \\ \frac{E}{1+\nu}(u_x + iu_y) &= (3-4\nu)\varphi(z) - z\overline{\varphi'(z)} - \overline{\psi(z)}, \end{aligned} \tag{2.65}$$

where overbar denotes complex conjugation. On the boundary $\partial\Pi$ the traction-free boundary condition transforms into

$$\varphi(\zeta) + \zeta\overline{\varphi'(\zeta)} + \overline{\psi(\zeta)} = f(\zeta) + C \qquad \text{for} \quad \zeta \in \partial\Pi, \tag{2.66}$$

where C is an arbitrary constant. The term on the right side represents surface forces and is given by

$$f(\zeta) = i\int_{s_0}^{s} (f_x + if_y)ds, \tag{2.67}$$

where $f = (-n_x, 0) = (\frac{dy}{ds}, 0)$ are surface forces appearing in eq. (2.58), thus

$$f(\zeta) = -iy(s), \tag{2.68}$$

because we have chosen s_0 so that $y(s_0) = 0$.

The periodicity of the stresses and displacements does not imply periodicity of Goursat functions φ, ψ in general. It is, however, possible to define new functions $\varphi_0(z), \psi_0(z)$ periodic in x, bounded as $y \to -\infty$ and uniquely determined to within two arbitrary constants

$$\varphi(z) = \varphi_0(z), \tag{2.69}$$

$$\psi(z) = \psi_0(z) - z\varphi_0'(z). \tag{2.70}$$

The boundary condition (2.66) becomes

$$\varphi_0(\zeta) + (\zeta - \overline{\zeta})\overline{\varphi_0'(\zeta)} + \overline{\psi_0(\zeta)} = f(\zeta) \qquad \text{for} \quad \zeta \in \partial\Pi, \tag{2.71}$$

where with $C = 0$ we have chosen on of the two additive constants for φ_0 and ψ_0.

Now all terms appearing in boundary condition (2.71) are periodic with wavelength λ. The domain Π can be transformed with $w = e^{iaz}, a = \frac{2\pi}{\lambda}$ to the exterior of a closed curve L (which contains the origin), Figure 2.3.

Functions

$$\Phi(w) = \varphi_0(\frac{1}{ia}\ln w), \tag{2.72}$$

$$\Psi(w) = \psi_0(\frac{1}{ia}\ln w), \tag{2.73}$$

$$\tag{2.74}$$

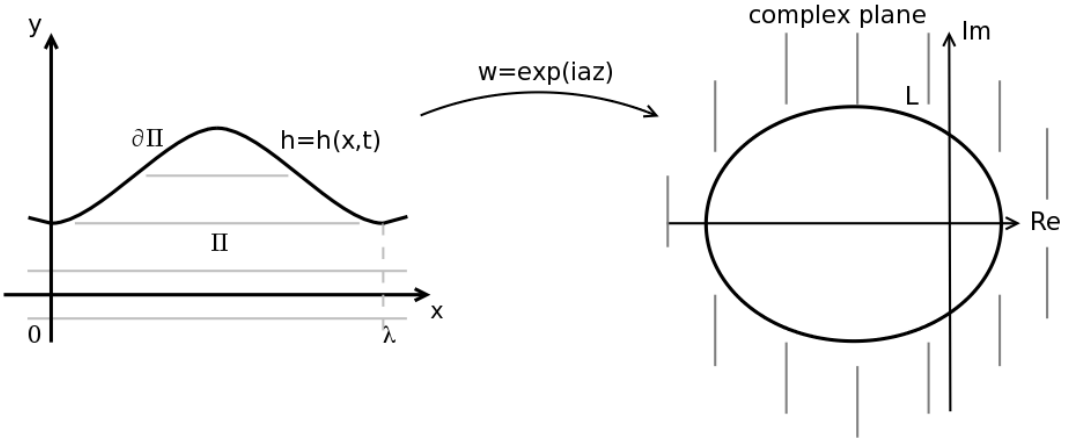

Figure 2.3: Transformation to the closed curve in the complex plane.

are analytic in the w plane exterior to the boundary L. Setting $\zeta = \frac{1}{ia}\ln\eta$ gives boundary condition (2.71) along L

$$\Phi(\eta) - 2\overline{\eta}\ln|\eta|\overline{\Phi'(\eta)} + \overline{\Psi(\eta)} = F(\eta), \quad \text{for} \quad \eta \in L, \tag{2.75}$$

where

$$F(\eta) = f(\frac{1}{ia}\ln\zeta) = i\frac{\ln|\eta|}{a}. \tag{2.76}$$

The elasticity problem is now solved with finding of two functions Φ, Ψ analytic outside L and satisfying boundary condition (2.75).

2.6.1 Boundary integral equation

With analyticity of Φ and Ψ, further reduction to a single nonsingular integral equation over L is possible. We replace the terms in (2.75) by their conjugates, multiply by $\frac{1}{2\pi i}\frac{\mathrm{d}\eta}{\eta - w_0}$ (w_0 is arbitrary inside L) and integrate counter-clockwise over L to get

$$\int_L \frac{\overline{\Phi(\eta)}}{\eta - w_0}\mathrm{d}\eta - 2\int_L \frac{\eta\ln|\eta|\Phi'(\eta)}{\eta - w_0}\mathrm{d}\eta + \int_L \frac{\Psi(\eta)}{\eta - w_0}\mathrm{d}\eta = 2\pi i A(w_0) \tag{2.77}$$

and

$$A(w_0) = \frac{1}{2\pi i}\int_L \frac{\overline{F(\eta)}}{\eta - w_0}\mathrm{d}\eta. \tag{2.78}$$

Since $\Phi(\eta)$ and $\Psi(\eta)$ are analytic outside of L, it holds

$$\frac{1}{2\pi i}\int_L \frac{\Phi(\eta)}{\eta - w_0}\mathrm{d}\eta = \Phi(\infty), \tag{2.79}$$

$$\frac{1}{2\pi i}\int_L \frac{\Psi(\eta)}{\eta - w_0}\mathrm{d}\eta = \Psi(\infty), \tag{2.80}$$

We set $\Psi(\infty) = 0$ (and thus the second arbitrary constant mentioned earlier) for simplicity. Differentiating (2.79) with respect to w_0 we get

$$\frac{1}{2\pi i}\int_L \frac{\Phi(\eta)}{(\eta - w_0)^2}\mathrm{d}\eta = 0, \tag{2.81}$$

and integrating by parts with respect to η we end with

$$\frac{1}{2\pi i}\int_L \frac{\Phi'(\eta)}{\eta - w_0}\mathrm{d}\eta = 0. \tag{2.82}$$

Conjugating (2.79) and substracting them for the point w_0 and origin 0 (both always inside L) we have

$$\frac{1}{2\pi i}\int_L \frac{\overline{\Phi(\eta)}}{\overline{\eta} - \overline{w_0}}\mathrm{d}\overline{\eta} - \frac{1}{2\pi i}\int_L \frac{\overline{\Phi(\eta)}}{\overline{\eta}}\mathrm{d}\overline{\eta} = 0. \tag{2.83}$$

Now we add the last equation and multiplications of (2.81), (2.82) (to ensure well-conditioned integral equation) to the boundary integral equation (2.77)

$$\begin{aligned}\frac{1}{2\pi i}\int_L \frac{\overline{\Phi(\eta)}}{\eta - w_0}\mathrm{d}\eta + \frac{1}{2\pi i}\int_L \frac{\overline{\Phi(\eta)}}{\overline{\eta} - \overline{w_0}}\mathrm{d}\overline{\eta} + \frac{1}{\pi i}\int_L \frac{(w_0 \ln|w_0| - \eta\ln|\eta|)\Phi'(\eta)}{\eta - w_0}\mathrm{d}\eta - \\ - \frac{1}{2\pi i}\int_L \frac{\overline{\Phi(\eta)}}{\overline{\eta}}\mathrm{d}\overline{\eta} - \frac{1}{2\pi i}\overline{\eta_0}\mathrm{Re}\left[\int_L \frac{\Phi(\eta)}{\eta^2}\mathrm{d}\eta\right] = A(w_0).\end{aligned} \tag{2.84}$$

Last step is to take the limit $w_0 \to \eta_0$ from inside L, and η_0 is a point on L. When we use the boundary values of Cauchy integrals, i.e.

$$\lim_{w_0\to\eta_0}\frac{1}{2\pi i}\int_L \frac{\Phi(\eta)}{\eta - w_0}\mathrm{d}\eta = \frac{1}{2}\Phi(\eta_0) + \frac{1}{2\pi i}(v.p.)\int_L \frac{\Phi(\eta)}{\eta - \eta_0}\mathrm{d}\eta \tag{2.85}$$

we get the resulting nonsingular integral equation for Φ

$$\begin{aligned}\overline{\Phi(\eta_0)} + \frac{1}{2\pi i}\int_L \overline{\Phi(\eta)}\mathrm{d}\left[\ln\frac{\eta - \eta_0}{\overline{\eta} - \overline{\eta_0}}\right] + \frac{1}{\pi i}\int_L \Phi(\eta)\mathrm{d}\left[\frac{\eta\ln|\eta| - \eta_0\ln|\eta_0|}{\eta - \eta_0}\right] + \\ + \frac{1}{2\pi i}\int_L \frac{\overline{\Phi(\eta)}}{\overline{\eta}}\mathrm{d}\overline{\eta} - \frac{1}{2\pi i}\overline{\eta_0}\mathrm{Re}\left[\int_L \frac{\Phi(\eta)}{\eta^2}\mathrm{d}\eta\right] = A(\eta_0)\end{aligned} \tag{2.86}$$

We make a trick adding zero to desingularize the right hand side

$$\begin{aligned}A(\eta_0) = \lim_{w_0\to\eta_0} A(w_0) = \frac{\overline{F(\eta_0)}}{2} + \frac{1}{2\pi i}(v.p.)\int_L \frac{\overline{F(\eta)}}{\eta - \eta_0}\mathrm{d}\eta \pm \\ \pm\frac{1}{2\pi i}(v.p.)\int_L \frac{\overline{F(\eta_0)}}{\eta - \eta_0}\mathrm{d}\eta = \frac{\overline{F(\eta_0)}}{2} + \frac{1}{2\pi i}\int_L \frac{\overline{F(\eta)} - \overline{F(\eta_0)}}{\eta - \eta_0}\mathrm{d}\eta + \\ + \frac{\overline{F(\eta_0)}}{2\pi i}(v.p.)\int_L \frac{1}{\eta - \eta_0}\mathrm{d}\eta = \overline{F(\eta_0)} + \frac{1}{2\pi i}\int_L \frac{\overline{F(\eta)} - \overline{F(\eta_0)}}{\eta - \eta_0}\mathrm{d}\eta,\end{aligned} \tag{2.87}$$

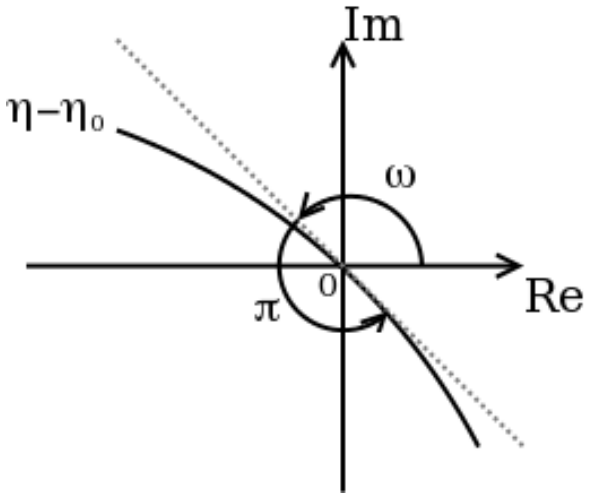

Figure 2.4: Boundary values of (2.88).

because (see Figure 2.4)

$$\frac{1}{2\pi i}(v.p.)\int_0^{2\pi}\frac{1}{\eta-\eta_0}\frac{\mathrm{d}(\eta-\eta_0)}{\mathrm{d}\theta}\mathrm{d}\theta=\frac{1}{2\pi i}\left[\ln|\eta-\eta_0|+i\arg(\eta-\eta_0)\right]_0^{2\pi}=\frac{1}{2} \tag{2.88}$$

Since the strain energy density S depends on Φ only (see (2.52), (2.69), (2.72)), Ψ is not required to determine surface evolution and we have

$$\begin{aligned}\varphi_0'(z) &= ia\eta\Phi'(\eta),\\ S &= \left[1+4\mathrm{Re}\left(ia\eta\Phi'(\eta)\right)\right]^2.\end{aligned} \tag{2.89}$$

2.6.2 Analytic continuation

In order to obtain stress tensor from equations (2.65), (2.69), (2.72) inside the film and the substrate, we have to construct analytic continuation of analytic functions Φ, Ψ and their first and second derivatives in the exterior of the curve L. Since they're bounded at infinity, we can use the Cauchy integral formula for the point ρ_i in the exterior of the curve L

$$\Phi(\rho_i)=\Phi(\infty)-\frac{1}{2\pi i}\int_L\frac{\Phi(\eta)}{\eta-\rho_i}\mathrm{d}\eta. \tag{2.90}$$

This is improper for numerical calculations, when the point ρ_i is close to the curve L. Therefore we add suitable zero (from residue theorem)

$$\frac{1}{2\pi i}\int_L\frac{\Phi(\eta_i)}{\eta-\rho_i}\mathrm{d}\eta=0, \tag{2.91}$$

to aid the accuracy of computations. We end up with the equation

$$\Phi(\rho_i)=\Phi(\infty)-\frac{1}{2\pi i}\int_L\frac{\Phi(\eta)-\Phi(\eta_i)}{\eta-\rho_i}\mathrm{d}\eta, \tag{2.92}$$

where $\rho_i \in \mathrm{Ext}L$ and $\Phi(\infty)$ is computed from (2.79) with $w_0 = 0$. The point η_i is nearest to ρ_i which lies on L.

First and second derivative of Φ outside L are obtained also with Cauchy integral formulae with "regularization" terms reminding of Taylor series

$$\Phi'(\rho_i) = -\frac{1}{2\pi i}\int_L \frac{\Phi(\eta) - \Phi(\eta_i) - (\eta-\eta_i)\Phi'(\eta_i)}{(\eta-\rho_i)^2}\mathrm{d}\eta, \tag{2.93}$$

and

$$\Phi''(\rho_i) = -\frac{1}{2\pi i}\int_L \frac{\Phi(\eta) - \Phi(\eta_i) - (\eta-\eta_i)\Phi'(\eta_i) - \frac{1}{2}(\eta-\eta_i)^2\Phi''(\eta_i)}{(\eta-\rho_i)^3}\mathrm{d}\eta, \tag{2.94}$$

since following integrals vanish because the integrated functions are holomorphic outside L

$$0 = -\frac{1}{2\pi i}\int_L \frac{\Phi(\eta_i) - (\eta-\eta_i)\Phi'(\eta_i)}{(\eta-\rho_i)^2}\mathrm{d}\eta, \tag{2.95}$$

$$0 = -\frac{1}{2\pi i}\int_L \frac{\Phi(\eta_i) - (\eta-\eta_i)\Phi'(\eta_i) - \frac{1}{2}(\eta-\eta_i)^2\Phi''(\eta_i)}{(\eta-\rho_i)^3}\mathrm{d}\eta. \tag{2.96}$$

Values of Ψ on the boundary are computed from (2.75) and then similar procedure is applied on Ψ in $\mathrm{Ext}L$ with $\Psi(\infty) = 0$.

2.7 Surface energy anisotropy

The anisotropy of the surface energy plays critical role in determining the equilibrium crystal shape (ECS). This was formulated as Wulff construction in two dimensions - convex envelope of the perpendiculars through the tip of each radius vector in a polar plot of $\gamma(\theta)$ describes crystal shape in equilibrium, Figure 2.5. It can have flat/curved sides connected smoothly or by corners. Flat sides correspond to facets and develop for $\gamma(\theta)$ with discontinuous first derivative at the minima (cusp), otherwise curved sides are formed. Corners develop for high surface anisotropy when the surface stiffnesses is negative for some orientations, Spencer (2004). The presence of cusps in $\gamma(\theta)$ depends on whether the system is below the thermal roughening temperature or not.

We will follow Long et al. (2001) in the notation of surface energy. Isotropic version is denoted γ_1, smoothly anisotropic γ_2, cusped anisotropic γ_3 with discontinuous derivative at $\beta\theta = n\pi, \quad n \in \mathbb{N}$ given by Bonzel and Preuss (1995) and its rounded version γ_4 used in the numerical calculations

$$\gamma_1(\theta) = 1, \tag{2.97}$$

$$\gamma_2(\theta) = 1 + g\sin^2(\beta\theta), \tag{2.98}$$

$$\gamma_3(\theta) = 1 + g|\sin(\beta\theta)|, \tag{2.99}$$

$$\gamma_4(\theta) = 1 + g\sqrt{G^{-2} + \sin^2(\beta\theta)}, \tag{2.100}$$

$$\gamma_{\mathrm{Te}}(\theta) = 1 - g\cos(\beta\theta), \tag{2.101}$$

$$\tag{2.102}$$

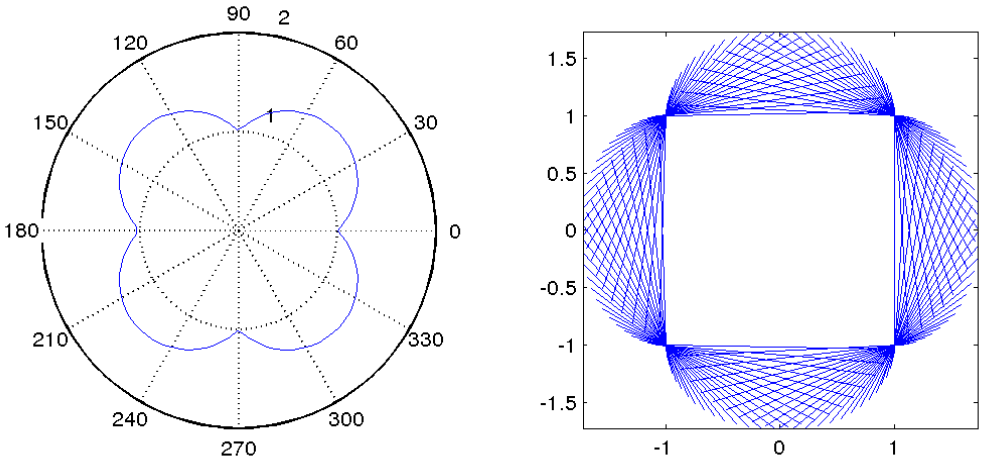

Figure 2.5: Polar graph of surface energy and its Wulff construction.

where β sets the minima, g sets the strength of anisotropy and $G = 500$ is a rounding parameter representing miscut angle $\approx 0.1°$. It is difficult to grow a perfect facet and real materials have usually slight miscut of the facet (we will call facet every nice approximation of the perfect one). This corresponds to a rounded version of the cusped surface energy γ_4 (2.97) used in the simulation studies of Eisenberg and Kandel (2005); Long et al. (2001). Tersoff et al. (2002) used the form γ_{Te} (which is equivalent to γ_2 for the same minima) to predict the prepyramid to pyramid phase transition. Let us denote

$$\Upsilon(\theta) = \gamma(\theta) + \frac{\partial^2 \gamma}{\partial \theta^2} \tag{2.103}$$

the nondimensional "surface stiffness", which appears at the equation (2.27) for chemical potential from the surface energy. Corresponding surface stiffnesses are then

$$\begin{aligned}
\Upsilon_1(\theta) &= 1, && (2.104)\\
\Upsilon_2(\theta) &= 1 + 2g\beta^2 - (4\beta^2 - 1)g\sin^2(\beta\theta), && (2.105)\\
\Upsilon_3(\theta) &= 1 - (\beta^2 - 1)g|\sin(\beta\theta)|, \text{ without singularities at } \beta\theta = 0, \pm\pi, && (2.106)\\
\Upsilon_4(\theta) &= 1 + g\sqrt{\varpi} + g\beta^2\frac{\cos(\beta\theta)}{\sqrt{\varpi}} - \frac{g\beta^2}{4}\frac{\sin^2(2\beta\theta)}{\varpi^{\frac{3}{2}}}, && (2.107)\\
\varpi &= G^{-2} + \sin^2(\beta\theta), && (2.108)\\
\Upsilon_{\mathrm{Te}}(\theta) &= 1 + (\beta^2 - 1)g\cos(\beta\theta). && (2.109)
\end{aligned}$$

The difference between Υ_4 and Υ_3 can be seen on Figure 2.6.

For simplicity, we will speak about weak anisotropy, if $\Upsilon(\theta) > 0$ for all angles θ and strong anisotropy, if $\Upsilon(\theta) < 0$ for some angles θ.

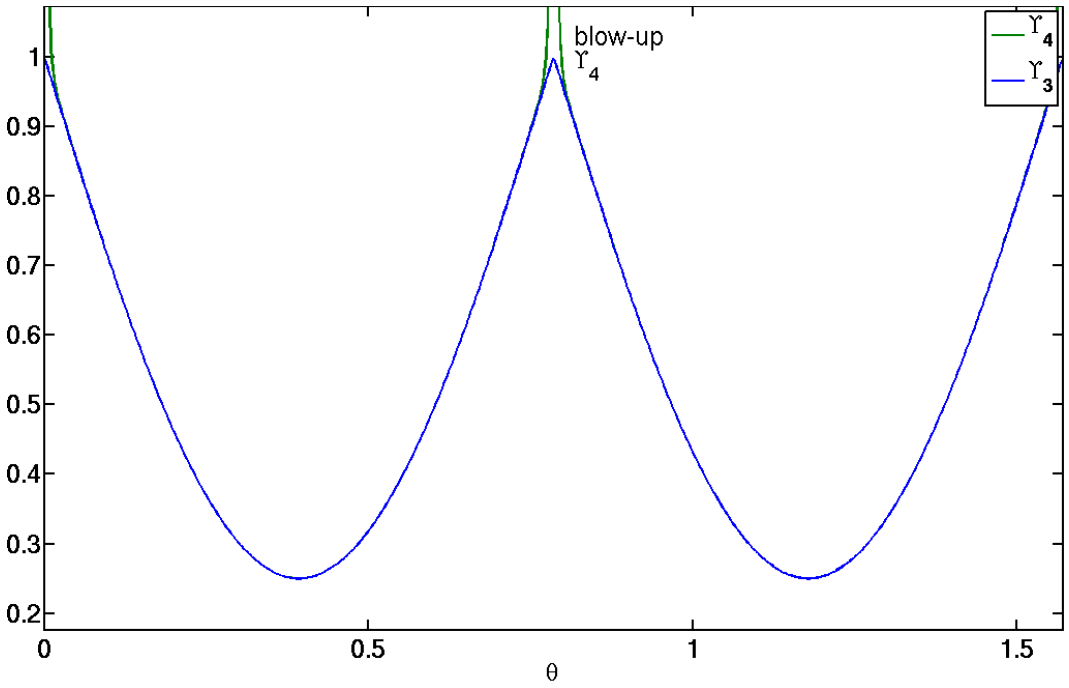

Figure 2.6: Cusped surface stiffness Υ_3 and its rounded version Υ_4.

2.8 Linear stability analysis

To determine the first order perturbation analysis of the evolution equation with wetting energy and smooth anisotropic surface energy, we will follow the approach of Srolovitz (1989). Anisotropy of the surface energy does not influence the wetting energy term if we consider perturbation to the flat film with $\theta = 0°$. It enters just the surface energy term as surface stiffness instead of the surface energy.

We perturb the flat film of height h_f with small sinusoidal perturbation (2.64) such that $p_0 a \ll 1$. Linearizing all the terms in (2.59), (2.60) we find

$$\frac{\partial h}{\partial t} = \frac{\partial^2}{\partial x^2}\left(-\Upsilon(0)h_{xx} + S - \frac{2b(\gamma_s - \gamma_f)}{\pi\gamma_f h_f^3}h\right), \tag{2.110}$$

where the strain energy density is given to the first order by Srolovitz (1989)

$$S = 1 - 4p_0 a\cos(ax). \tag{2.111}$$

Thus initially the perturbation evolves according to

$$\frac{\partial p_0}{\partial t} = \underbrace{a^2\left(4a - \Upsilon(0)a^2 - \frac{2b(\gamma_s - \gamma_f)}{\pi\gamma_f h_f^3}\right)}_{\varsigma-\text{growth rate}} p_0. \tag{2.112}$$

If the film wets the substrate ($\gamma_s - \gamma_f > 0$, Stranski-Krastanow mode) and

$$h_f < h_c = \left(\Upsilon(0)\frac{b(\gamma_s - \gamma_f)}{2\pi\gamma_f}\right)^{1/3}, \tag{2.113}$$

the film is stable against any small perturbations and otherwise unstable for wavenumbers in the range

$$a^- < a < a^+, \quad a^\pm = \frac{2 \pm \sqrt{4 - \Upsilon(0)\frac{2b(\gamma_s-\gamma_f)}{\pi\gamma_f h_f^3}}}{\Upsilon(0)}. \tag{2.114}$$

The initially fastest growing wavenumber a_f is that with maximum growth rate, which can be obtained by solving

$$\frac{\mathrm{d}\varsigma}{\mathrm{d}a} = 4a\left(3a - \Upsilon(0)a^2 - \frac{b(\gamma_s-\gamma_f)}{\pi\gamma_f h_f^3}\right) = 0, \tag{2.115}$$

which gives

$$a_f = \frac{3 + \sqrt{9 - 4\Upsilon(0)\frac{b(\gamma_s-\gamma_f)}{\pi\gamma_f h_f^3}}}{2\Upsilon(0)}, \tag{2.116}$$

because the other solution corresponds to the minimum growth rate. This is in agreement with previous works for isotropic surface energy with or without the wetting energy by Chiu and Gao (1995); Tekalign and Spencer (2004); Pang and Huang (2006) but was not considered with anisotropic surface energy before. Initial self-similar evolution of the sinusoidal perturbation can be therefore seen also for anisotropic surface energy.

If the substrate wets the film ($\gamma_s - \gamma_f < 0$) any perturbation will grow and islands tend to form from the very beginning as in the Volmer-Weber mode. If there is no mismatch or it is very small (e.g. for $\mathrm{In}_x\mathrm{Ga}_{1-x}\mathrm{As/GaAs}$ system) and $\gamma_s - \gamma_f > 0$, the film is always stable and layer-by-layer Frank-van der Merwe growth mode is observed. Also basic three growth modes can be explained with the wetting energy.

2.9 Material parameters

To illustrate the characteristic physical quantities, we consider Ge thin film on $\mathrm{Si}_{0.5}\mathrm{Ge}_{0.5}(001)$ substrate and InAs/GaAs(001). Material parameters can be seen on Table 2.1.

The mismatch strain ε_0 for Ge/Si system is 2.09%. For parameters of the substrate we take the weighted average of values for Ge and Si, $E = 117$ GPa, $\tilde{\gamma}_s = 2.22\ \mathrm{Nm}^{-1}$, $\nu = 0.276$. This gives characteristic length $l_0 = 79$ nm. For the film we have $\tilde{\gamma}_f = 1.9\ \mathrm{Nm}^{-1}$. Rough estimate of the characteristic time depends on the constant

$$D = \frac{\nu_S D_S V_{at}^2}{k_B \Theta}. \tag{2.117}$$

For the atomic volume of Ge (8 atoms per unit cell) we have

$$V_{at} = \frac{a_{Ge}^3}{8} = 2.3 \cdot 10^{-29}\mathrm{m}^3. \tag{2.118}$$

Parameter	Ge	Si	InAs	GaAs
a[Å]	5.66	5.43	6.06	5.75
E[GPa]	103	130	52	88
ν	0.27	0.28	0.35	0.31
$\tilde{\gamma}$[Nm^{-1}]	1.9	2.5	0.75	0.9

Table 2.1: Lattice constant is denoted a, Young modulus E, Poisson ratio ν and surface energy $\tilde{\gamma}$. Values are taken from Spencer et al. (2001) and Penev (2002).

For the number of atoms per surface area it holds (2 atoms on side of unit cell)

$$\nu_S = \frac{2}{a_{Ge}^2} = 6.2 \cdot 10^{18}\mathrm{m}^{-2}. \tag{2.119}$$

Typical temperature in experiments Medeiros-Ribeiro et al. (1998); Ross et al. (1998) is $\Theta \approx 900$ K and surface diffusion constant $D_S = 10^{-13}$ m^{2}s^{-1} Eisenberg and Kandel (2002); Spencer et al. (2001). With these values and Boltzmann constant $k_B = 1.38{\cdot}10^{-23}$ Jmol^{-1}K^{-1} we obtain $D = 2.6{\cdot}10^{-32}$ N^{-1}m^{5}s^{-1} and characteristic time $\tau_0 = 0.1$ s. The competition between strain and surface energies is therefore important in typical growth experiments. Value of the characteristic time is uncertain because the surface diffusion constant is not experimentally well known and varies with temperature. It is well known that square pyramid islands on Si(001) have facets at (105), Mo et al. (1990), what implies facet angles $0°, \pm 11°$ and thus $\beta = 16$ for the surface energy.

The InAs/GaAs(001) system has greater mismatch $\varepsilon_0 = 0.07$. This gives characteristic length $l_0 = 5.5$ nm. Facet angles $0°, \pm 45°, \pm 90°$ are seen for this system, corresponding to $\beta = 4$.

All numerical results will be presented in the nondimensional units if not otherwise stated.

Chapter 3

Numerical methods

Solution to the elasticity problem on the surface is obtained by numerical quadrature of the boundary integral equation and then analytically continued inside the film. Evolution problem is formulated numerically using finite element and spectral methods.

3.1 Elasticity problem

We will solve the integral equation (2.86) by numerical quadrature. Smooth boundary L is taken as a set of N points $\eta_j, j = 1, \ldots, N$ parametrized by equidistant grid $\theta_j = \frac{2\pi}{N}(j-1), j = 1, \ldots, N$ and $\theta \in (0, 2\pi), \Delta\theta = \frac{2\pi}{N}$. All integrals over η are converted to θ with trapezoidal rule, e.g.

$$\int_L \frac{\Phi(\eta)}{\eta^2}\mathrm{d}\eta = \int_L \frac{\Phi(\eta(\theta))}{\eta(\theta)^2}\frac{\mathrm{d}\eta}{\mathrm{d}\theta}\mathrm{d}\theta = \frac{2\pi}{N}\sum_{j=1}^{N}\frac{\Phi(\eta_j)}{\eta_j^2}\eta_j' + O(\Delta\theta^2), \tag{3.1}$$

where $\eta_j' = \frac{\mathrm{d}\eta}{\mathrm{d}\theta}(\theta_j)$.

Approximated integral equation is evaluated at the N node points $\eta_0 = \eta_j$ and we obtain N complex equations for the N unknowns $\Phi_j = \Phi(\eta_j)$

$$\begin{aligned}\overline{\Phi_j} + \frac{1}{iN}\sum_{k=1}^{N}\left[\overline{\Phi_k}\frac{\mathrm{d}o_k}{\mathrm{d}\theta} + 2\Phi_k\frac{\mathrm{d}p_k}{\mathrm{d}\theta} + \frac{\overline{\Phi_k}}{\overline{\eta_k}}\frac{\mathrm{d}\overline{\eta_k}}{\mathrm{d}\theta} - \frac{\overline{\eta_j}}{2}(\Phi_k w_k + \overline{\Phi_k}\,\overline{w_k})\right] = \\ = \overline{F_j} + \frac{1}{iN}\sum_{k=1}^{N}\frac{\overline{F_k} - \overline{F_j}}{\eta_k - \eta_j}\frac{\mathrm{d}\eta_k}{\mathrm{d}\theta}, \quad j = 1, \ldots, N,\end{aligned} \tag{3.2}$$

where we have written for simplicity

$$o(\eta) = \ln\frac{\eta - \eta_0}{\overline{\eta} - \overline{\eta_0}}, \tag{3.3}$$

$$p(\eta) = \frac{\eta\ln|\eta| - \eta_0\ln|\eta_0|}{\eta - \eta_0}, \tag{3.4}$$

$$w(\eta) = \frac{1}{\eta^2}\frac{\mathrm{d}\eta}{\mathrm{d}\theta}. \tag{3.5}$$

We separate real and imaginary parts of the unknowns $\Phi_j = \mathrm{Re}(\Phi_j) + i\mathrm{Im}(\Phi_j)$ and get a system of $2N$ real linear equations for $\mathrm{Re}(\Phi_j), \mathrm{Im}(\Phi_j)$ and we solve with GMRES iterative solver. This is the most expensive step in our calculations.

Derivatives and limits in the discretized equation (3.2) at the point $\eta_0 = \eta_j$ (singular at first sight) are computed using l'Hospital rule (even more than once)

$$\lim_{\eta\to\eta_j} \frac{\mathrm{d}\left[\ln\frac{\eta-\eta_j}{\overline{\eta}-\overline{\eta_j}}\right]}{\mathrm{d}\theta} = i\mathrm{Im}\left[\frac{\eta_j''}{\eta_j'}\right], \tag{3.6}$$

$$\lim_{\eta\to\eta_j} \frac{\mathrm{d}\left[\frac{\eta\ln|\eta|-\eta_j\ln|\eta_j|}{\eta-\eta_j}\right]}{\mathrm{d}\theta} = q_j' + \frac{\eta_j q_j''}{2\eta_j'} - \frac{\eta_j\eta_j''q_j'}{2(\eta_j')^2}, \tag{3.7}$$

$$\lim_{\eta\to\eta_j} \frac{\overline{F}-\overline{F_j}}{\eta-\eta_j} = \frac{\mathrm{d}F}{\mathrm{d}\eta}(\eta_j) \tag{3.8}$$

where we denoted

$$q(\eta) = \ln|\eta|, \qquad q_j' = \frac{\mathrm{d}q}{\mathrm{d}\eta}(\eta_j)\frac{\mathrm{d}\eta}{\mathrm{d}\theta}(\theta_j). \tag{3.9}$$

Obtaining the analytic continuation in the exterior of L is straightforward with (2.92), (2.93). We choose the lower bound e on the y axis, make vertical line from $h(x_i)$ and divide the section between e and h_i into N_2 intervals. This grid of points $p_{kj} = x_k + iy_j$ is equidistant in x and nonuniform in y. With transformation $w_{kj} = e^{iap_{ij}}$, we obtain points in exterior of L, for which we apply (2.92), (2.93).

Derivatives of 2π-periodic complex functions with respect to θ are computed with Fourier transform using its well known property

$$\widehat{f}(\omega) = \frac{1}{\sqrt{2\pi}}\int_{-\infty}^{-\infty} f(x)e^{-i\omega x}\mathrm{d}x, \quad f\in L^1(R) \tag{3.10}$$

$$\widehat{f'}(\omega) = i\omega\widehat{f}(\omega). \tag{3.11}$$

Fourier transform is computed on the discrete grid using the Discrete Fourier transform (DFT), especially with Fast Fourier transform (FFT) algorithm Weideman and Reddy (2000), e.g.

$$\eta_j^{\mathrm{DFT}} = \sum_{k=1}^{N} \eta_k e^{-\frac{2\pi i}{N}(j-1)(k-1)}, \quad \mathrm{DFT} \tag{3.12}$$

$$\frac{\mathrm{d}\eta_j}{\mathrm{d}\theta} = \frac{1}{N}\sum_{k=1}^{N} i\upsilon_k\eta_k^{\mathrm{DFT}} e^{\frac{2\pi i}{N}(j-1)(k-1)}, \quad \text{inverse DFT}, \tag{3.13}$$

where υ is the wavenumber vector

$$\upsilon = \left(0, 1, \ldots, \frac{N-2}{2}, -\frac{N}{2}, -\frac{N-2}{2}, \ldots, -1\right), \quad N \quad \text{even}, \tag{3.14}$$

and we take N as powers of 2 to speed-up the computations of DFT.

3.2 Evolution equation

We will use the strain energy density computed from Section 2.6 and solve the evolution equations (2.59), (2.60) in the weak form with Galerkin semidiscrete approximation using finite elements or using spectral methods.

3.2.1 Weak formulation

Since we have periodic Dirichlet and periodic Neumann conditions for h and flux, we require functions to have equal values on the boundary. Hence we choose the test space of functions from the Sobolev space $D = W^{1,2}_{per}(\Omega)$ with periodic values at the boundary. For a fixed time t, multiplying the equation for κ (2.59) with test function u and integrating per partes over the domain Ω we get

$$\begin{aligned}\int_\Omega \kappa(x,t)u(x)\mathrm{d}x = -\left[\frac{1}{\sqrt{1+h_x^2}}\frac{\partial h}{\partial x}(x,t)u(x)\right]_0^\lambda + \\ + \int_\Omega \frac{1}{\sqrt{1+h_x^2}}\frac{\partial h}{\partial x}(x,t)\frac{\mathrm{d}u}{\mathrm{d}x}(x)\mathrm{d}x, \quad \forall u \in D.\end{aligned} \tag{3.15}$$

From the periodic Neumann condition (2.62) for h, the boundary term vanishes.

With the same procedure on (2.60), we have

$$\begin{aligned}\int_\Omega \frac{\partial h}{\partial t}(x,t)w(x)\mathrm{d}x = \int_\Omega j_d(x,t)w(x)\mathrm{d}x + \left[\frac{1}{\sqrt{1+h_x^2}}\frac{\partial \mu}{\partial x}(x,t)w(x)\right]_0^\lambda - \\ - \int_\Omega \frac{1}{\sqrt{1+h_x^2}}\frac{\partial \mu}{\partial x}(x,t)\frac{\mathrm{d}w}{\mathrm{d}x}(x)\mathrm{d}x, \quad \forall w \in D,\end{aligned} \tag{3.16}$$

where the boundary term vanishes the same way with the use of periodic flux boundary condition (2.63).

Also more precisely, we are looking for $\kappa, h \in C^1(\langle 0,T\rangle; D)$ such that

$$\int_\Omega \kappa(t)u\mathrm{d}x = \int_\Omega \frac{1}{\sqrt{1+(h(t))_x^2}}\frac{\partial h(t)}{\partial x}\frac{\mathrm{d}u}{\mathrm{d}x}\mathrm{d}x, \quad \forall u \in D, \tag{3.17}$$

$$\int_\Omega \frac{\mathrm{d}h}{\mathrm{d}t}(t)w\mathrm{d}x = \int_\Omega j_d(t)w\mathrm{d}x - \int_\Omega \frac{1}{\sqrt{1+(h(t))_x^2}}\frac{\partial \mu(t)}{\partial x}\frac{\mathrm{d}w}{\mathrm{d}x}\mathrm{d}x, \tag{3.18}$$

for $\forall w \in D$. With N-dimensional subspace D_N of the test space D, we define the discrete problem: find functions $\kappa_N, h_N \in C^1(\langle 0,T\rangle; D_N)$ so that

$$\int_\Omega \kappa_N(t)u_N\mathrm{d}x = \int_\Omega \frac{1}{\sqrt{1+(h_N(t))_x^2}}\frac{\partial h_N(t)}{\partial x}\frac{\mathrm{d}u_N}{\mathrm{d}x}\mathrm{d}x, \quad \forall u_N \in D_N \tag{3.19}$$

and

$$\int_\Omega \frac{\mathrm{d}h_N}{\mathrm{d}t}(t) w_N \mathrm{d}x = \int_\Omega j_{dN}(t) w_N \mathrm{d}x - \int_\Omega \frac{1}{\sqrt{1+(h_N(t))_x^2}} \frac{\partial \mu_N(t)}{\partial x} \frac{\mathrm{d}w_N}{\mathrm{d}x} \mathrm{d}x \quad (3.20)$$

$\forall w_N \in D_N$.

Existence of the solution and convergence of the numerical scheme was not addressed here due to the different orientation of the work. To our best knowledge, some results exists just for mean curvature flow (second order flow) and Willmore flow (fourth order) with no strain energy and other terms present here.

3.2.2 Finite element method

Let us assume the triangulation $\mathcal{T}_d$ of the domain Ω with N elements $\Omega_i = \langle x_i, x_{i+1} \rangle, i = 1, \ldots, N$. The $N+1$ nodes are $0 = x_1 < x_2 < \ldots < x_{N+1} = \lambda$, with $\triangle_i = x_{i+1} - x_i$ and maximal element diameter d. The space $D_d \subset D$ will consist of continuous functions on Ω with periodic values at x_1, x_{N+1}, linear on each element Ω_i with basis functions $\{\phi_i\}_{i=1}^N$ such that for $i = 1, \ldots, N$ and $j = 1, \ldots, N+1$ holds $\phi_i(x_j) = \delta_{ij}$ except $\phi_1(x_{N+1}) = 1$.

Interpolation operator $\mathcal{I}_d : C^0(\Omega) \to D_d$ is given by

$$\mathcal{I}_d h = \sum_{i=1}^{N+1} h_i \phi_i(x). \quad (3.21)$$

Values at the node points will be denoted as vector $\overline{h} = (h_1, h_2, \ldots, h_{N+1})$ in the following. We set $h_{N+1} = h_1$ in each time step to get periodic Dirichlet condition.

The usual L^2 scalar product on Ω will be written as $(\cdot, \cdot)$. The mass matrix M_d is given by

$$(M_d)_{ij} = (\phi_i, \phi_j) = \sum_{e=1}^{N} (\phi_i, \phi_j)_{\Omega_e} = \sum_{e=1}^{N} M_{ij}^{(e)}, \quad (3.22)$$

where subscript denotes restriction of the scalar product on element Ω_e. Since basis function ϕ_i is nonzero only in $\Omega_{i-1} \cup \Omega_i$, we easily compute

$$M_{ij}^{(e)} = \begin{pmatrix} \ddots & \vdots & \vdots & \\ \cdots & m_{e,e} & m_{e,e+1} & \cdots \\ \cdots & m_{e+1,e} & m_{e+1,e+1} & \cdots \\ & \vdots & \vdots & \ddots \end{pmatrix}, \quad (3.23)$$

where other terms than written are zero. This matrix is usually written as element mass matrix

$$\tilde{M}^{(e)} = \begin{pmatrix} m_{e,e} & m_{e,e+1} \\ m_{e+1,e} & m_{e+1,e+1} \end{pmatrix} = \frac{\Delta_e}{6} \begin{pmatrix} 2 & 1 \\ 1 & 2 \end{pmatrix}. \quad (3.24)$$

which follows from trivial integration of linear functions.

In the very same way, the weighted stiffness matrix is computed by elements

$$(L_d(\overline{h}))_{ij} = \left(\frac{\nabla\phi_i}{\sqrt{1+\overline{h}_x^2}}, \nabla\phi_j \right) = \sum_{e=1}^{N} \left(\frac{\nabla\phi_i}{\sqrt{1+\overline{h}_x^2}}, \nabla\phi_j \right)_{\Omega_e} = \sum_{e=1}^{N} (L_d(\overline{h}))_{ij}^{(e)} \tag{3.25}$$

with element stiffness matrix

$$\tilde{L}_d(\overline{h})^{(e)} = \frac{1}{\sqrt{1+(\overline{h}'_e)^2}} \frac{1}{\Delta_e} \begin{pmatrix} 1 & -1 \\ -1 & 1 \end{pmatrix} \tag{3.26}$$

and the derivative of h at the element e as

$$\overline{h}'_e = \frac{\overline{h}_{e+1} - \overline{h}_e}{\Delta_e}. \tag{3.27}$$

Inserting our finite element space D_d in the weak formulation (3.19), (3.20) and interpolating function μ also in this space we have

$$(\kappa_d, u_d) = \left(\frac{\nabla h_d}{\sqrt{1+(h_d)_x^2}}, \nabla u_d \right), \quad \forall u_d \in D_d, \tag{3.28}$$

$$\left(\frac{\mathrm{d}h_d}{\mathrm{d}t}, w_d \right) = (j_d, w_d) - \left(\frac{\nabla \mu_d}{\sqrt{1+(h_d)_x^2}}, \nabla w_d \right), \quad \forall w_d \in D_d, \tag{3.29}$$

where the variables are all time dependent. With the choice $w_d \equiv 1$, we have explicit mass conservation

$$\int_\Omega \frac{\mathrm{d}h_d}{\mathrm{d}t}(x)\mathrm{d}x = \int_\Omega j_d(x)\mathrm{d}x. \tag{3.30}$$

In the matrix form it holds (for every time t, which we have omitted for clarity)

$$M_d \overline{\kappa}_d = L_d(\overline{h}_d)\overline{h}_d, \tag{3.31}$$

$$M_d \frac{\mathrm{d}\overline{h}_d}{\mathrm{d}t} = M_d \overline{j}_d - L_d(\overline{h}_d)\overline{\mu}_d(\overline{h}_d), \tag{3.32}$$

$$\overline{\mu}_d(\overline{h}_d) = \Upsilon_d(\overline{h}_d)\overline{\kappa}_d + \overline{S}(\overline{h}_d) + \overline{\mu}_{wet}(\overline{h}_d) + \overline{\mu}_{cor}(\overline{h}_d), \tag{3.33}$$

where we introduced matrix $(\Upsilon_d)_{ij} = \delta_{ij}\overline{\Upsilon}$ with δ_{ij} Kronecker delta matrix. All matrices are sparse and this was used in the numerics to lower the memory usage.

The time interval $I = \langle 0, T\rangle$ is divided into intervals $I_k = \langle t_k, t_{k+1}\rangle$ with $t_{k+1} = t_k + \tau_k$ for time increments $\tau_k > 0, k = 0, 1, \ldots, K-1$.

This system of ordinary differential equations for $\overline{h}_d(t)$ is very stiff (owing to the curvature and regularization terms) and therefore we have used TR-BDF2 method which is one step, second order and both A- and L-stable Bank

et al. (1985) implemented in Matlab with function `ode23tb` (with automatic error and timestep control). The strain energy density is computed explicitly to enhance the computation speed, since most of the time is spent there.

We will show the TR-BDF2 algorithm on the general ODE system to simplify the writing

$$\mathbf{y}' = \mathbf{f}(\mathbf{y}), \tag{3.34}$$
$$\mathbf{y}(0) = \mathbf{y_0} \tag{3.35}$$

First divide each time interval τ_k into two parts, $\vartheta\tau_k$ and $(1-\vartheta)\tau_k$. Trapezoidal rule (TR) is then used in the first sub-interval

$$\frac{\mathbf{y}_{TR}^{k+1} - \mathbf{y}^k}{\vartheta\tau_k} = \frac{\mathbf{f}(\mathbf{y}_{TR}^{k+1}) + \mathbf{f}(\mathbf{y}^k)}{2} \tag{3.36}$$

and backward differentiation formula of order 2 is used in the second

$$\frac{1}{\tau_k}\left(\frac{2-\vartheta}{1-\vartheta}\mathbf{y}^{k+1} - \frac{1}{\vartheta(1-\vartheta)}\mathbf{y}_{TR}^{k+1} + \frac{1-\vartheta}{\vartheta}\mathbf{y}^k\right) = \mathbf{f}(\mathbf{y}^{k+1}) \tag{3.37}$$

Additionally, if ϑ is chosen properly it can be shown that the Jacobian need not be re-factored for the TR step, substantially reducing the CPU time per timestep. Local truncation error is estimated for each component and it is kept with relative error tolerance 10^{-3}, meaning that the we have all solution components with 0.1% relative error. Newton method is used for the solution of nonlinear equations. From higher order methods (although slower), numerical differentiation formula (NDF) method `ode15s` of order 5 was used for comparison.

3.2.3 Spectral methods

Another approach to the solution of the evolution equation uses periodicity and symmetry of the solutions Spencer and Meiron (1994). It enjoys infinite order of accuracy for smooth solutions. We will use truncated Fourier series to approximate the solution in the form

$$h(x_j, t) = h_j(t) = \sum_{l=0}^{N/2} c_l(t) \cos\left(\frac{2\pi l}{\lambda} x_j\right), \tag{3.38}$$

where we use equidistant grid $x_j = \frac{\lambda}{N}(j-1), j = 1, \ldots, N$. Now the time derivative in the evolution equation (2.60) can be written as

$$\frac{\mathrm{d}h_j(t)}{\mathrm{d}t} = \sum_{l=0}^{N/2} \frac{\mathrm{d}c_l(t)}{\mathrm{d}t} \cos\left(\frac{2\pi l}{\lambda} x_j\right) \tag{3.39}$$

and the problem can be solved in the Fourier space for $c_l(t)$ instead of $h_j(t)$. Spectral coefficients r_l are computed with the discrete Fourier transform

$$\left[j_d + \frac{\partial}{\partial x}\left(\frac{1}{\sqrt{1+h_x^2}}\frac{\partial \mu}{\partial x}\right)\right](x_j, t) = \sum_{l=0}^{N/2} r_l(t) \cos\left(\frac{2\pi l}{\lambda} x_j\right). \tag{3.40}$$

Also comparing (3.39) and (3.40) it must hold

$$\frac{\mathrm{d}c_l(t)}{\mathrm{d}t} = r_l(t), \quad l = 0, \ldots, \frac{N}{2}. \tag{3.41}$$

This ODE system is also very stiff and can be solved easily by the default TR-BDF2 only for $N \approx 100$ spectral coefficients, because for higher modes it is not possible to estimate them as accurately as the lower ones and we had to set lower absolute error tolerance on them. The way out from this could be semi-implicit algorithm, where nonlinear terms are treated explicitly and linear implicitly. This was not possible because the stiff terms were nonlinear.

We have also used implicit method of backward Euler differentiation. We start with initial surface profile $h_0(x)$, transform it into the spectral coefficients c_l^0 with FFT and start with iterations: for $k = 0, 1, \ldots$ find c_l^{k+1} such that

$$\frac{c_l^{k+1} - c_l^k}{\tau_k} = r_l^{k+1}. \tag{3.42}$$

System of nonlinear equations has to be solved in each timestep using Newton method. As different time scales play important role in the problem, we have adjusted the step size according to the well-known step-doubling procedure, but we experienced problems to capture the important events during evolution (shape transitions).

Pseudospectral method (e.g. Boyd (2001)) was developed similarly to the spectral but it computes the derivatives by Fourier differentiation as in (3.12) and solves the system of ODEs for $\overline{h}$ with the same TR-BDF2 scheme as for the finite element method. This algorithm performs qualitatively similar to FEM and implicitly contains periodic boundary conditions.

Chapter 4

Simulation results

We compare calculations of strain energy on the surface and inside islands with previous analytical and numerical results. Numerical schemes for evolution of islands reproduce known results of cusp formation (no wetting), ripening (with wetting) for isotropic surface energy. Deposition can have significant effect on film evolution. Smooth and cusped anisotropic surface energy is studied to see the facet formation and metastability of faceted island array, qualitatively comparable to experiments.

4.1 Strain energy

4.1.1 Numerical check - cycloid surface

Analytic result for the strain energy density of the 2π-periodic cycloid interface is known from Chiu and Gao (1993) for $\theta \in (0, 2\pi)$ and $0 \leq \alpha \leq 1$

$$\begin{aligned} x &= \theta + \alpha \sin\theta, && (4.1)\\ h(x) &= \alpha \cos\theta, && (4.2)\\ \theta_j &= \frac{2\pi}{N}(j-1), \quad j = 1, \ldots, N, && (4.3)\\ S^{exact}(\theta_j) &= \left(\frac{1-\alpha^2}{1+2\alpha\cos\theta_j+\alpha^2}\right)^2. && (4.4) \end{aligned}$$

We obtained spectral accurate results within standard error $err = 10^{-10}$ for the parameter $\alpha = 0.1, 0.5, 0.9$ (characterizing sharpness of the cusp) with $N = 16, 32, 256$ points

$$err = \sqrt{\frac{1}{N}\sum_{j=1}^{N}(S_j^{exact} - S_j^{num})^2}, \tag{4.5}$$

where we have computed the numerical value of the strain energy density S^{num} from (2.89) solving the integral equation for Φ. Sample cycloid surface and its strain energy is plotted on Figure 4.1.

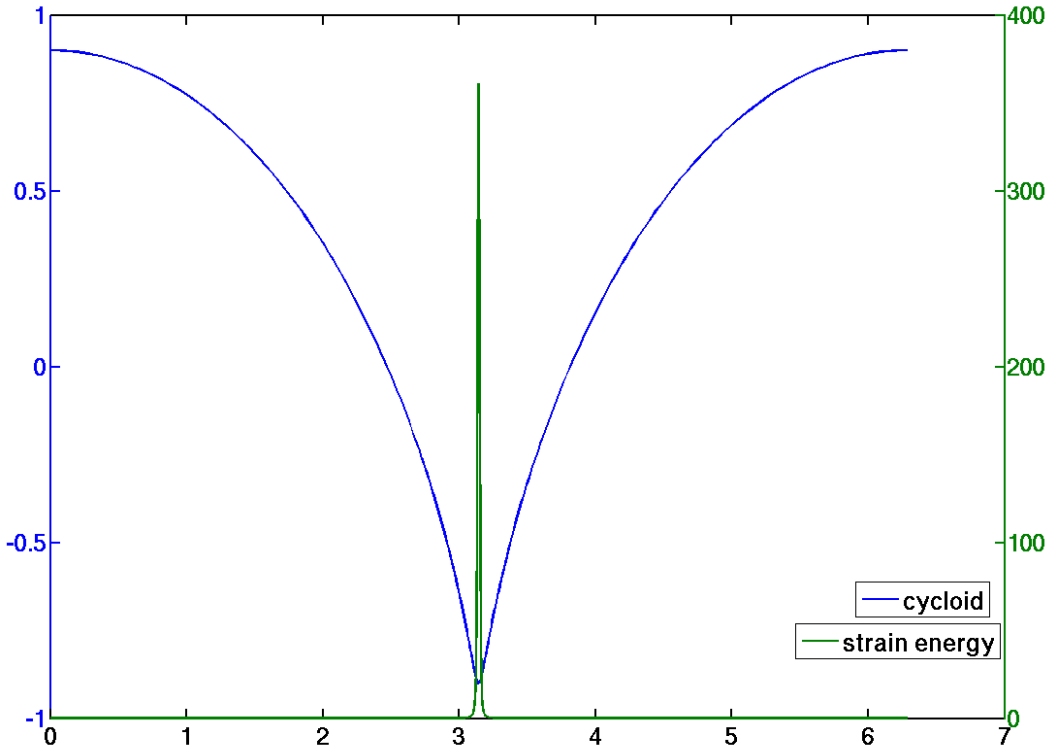

Figure 4.1: Strain energy density for the cycloid surface, $\alpha = 0.9$.

4.1.2 Stresses inside film and substrate

We have computed the components of stress tensor σ_{ij} according to the procedure in section 2.6.2 for one stable island (Figure 4.2) and T-pyramid (Figure 4.3).

In agreement with Spencer and Tersoff (2001), we observe misfit stress (σ_{xx}) relaxation at the top of island, which can be eventually overrelaxed for big islands. The thin inter-island wetting layer stays quite uniformly strained as for the case of flat film. Island edges experience big stress concentration, which can lead to the introduction of dislocations. Substrate is deformed because of the island relaxation and therefore opposite misfit stress is present directly below the island. Other elements of the stress tensor (σ_{xy}, σ_{yy}) are small generally, decaying in the substrate.

4.2 Isotropic surface energy

We present justification of our evolution numerical schemes for (2.59),(2.60) with well known results for isotropic surface energy (and thus stiffness) $\Upsilon_1 = 1$.

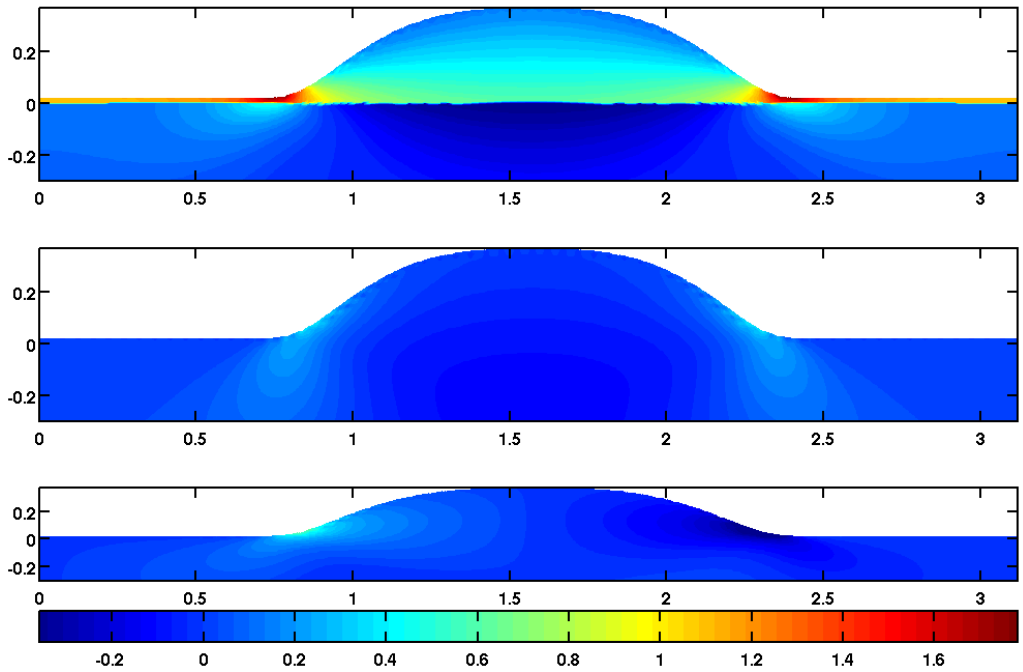

Figure 4.2: Components of stress tensor σ_{xx} (upper), σ_{yy} (middle) and σ_{xy} (lower) inside the stable quantum dot ($y > 0$) and in the substrate ($y < 0$). The dot was taken from calculations stable island array for cusped surface energy Υ_3 with $b = 5 \cdot 10^{-3}$.

4.2.1 Linear equation without strain energy

Omitting strain energy term, linearizing curvature ($\kappa = -h_{xx}$) and small slope approximation ($h_x \ll 1$) in (2.60), we in fact solve linear diffusion equation of fourth order

$$\frac{\partial h}{\partial t} = -\frac{\partial^4 h}{\partial x^4} \quad \text{in} \quad \langle 0, \lambda \rangle \times \langle 0, T \rangle \tag{4.6}$$

$$\frac{\partial h}{\partial x}(0,t) = \frac{\partial h}{\partial x}(\lambda, t) = 0, \tag{4.7}$$

$$h(x,0) = \cos(ax), a = \frac{2\pi}{\lambda}, \tag{4.8}$$

which is analytically solvable using Fourier transformation (3.10)

$$\frac{\mathrm{d}\widehat{h}}{\mathrm{d}t}(\omega,t) = -(i\omega)^4 \widehat{h}(\omega,t), \tag{4.9}$$

$$\widehat{h}(\omega,t) = \widehat{h}(\omega,0) e^{-\omega^4 t}, \tag{4.10}$$

$$\widehat{h}(\omega,0) = \sqrt{2\pi}\frac{\delta(\omega - a) + \delta(\omega + a)}{2}, \tag{4.11}$$

$$h(x,t) = e^{-a^4 t}\cos(ax), \tag{4.12}$$

where here δ indicated Dirac delta distribution. With our numerical schemes, standard error (4.5) 10^{-3} of h from analytical solution was obtained with $N = 50$. Uniform space grid, $a = 1, T = 1$ was used.

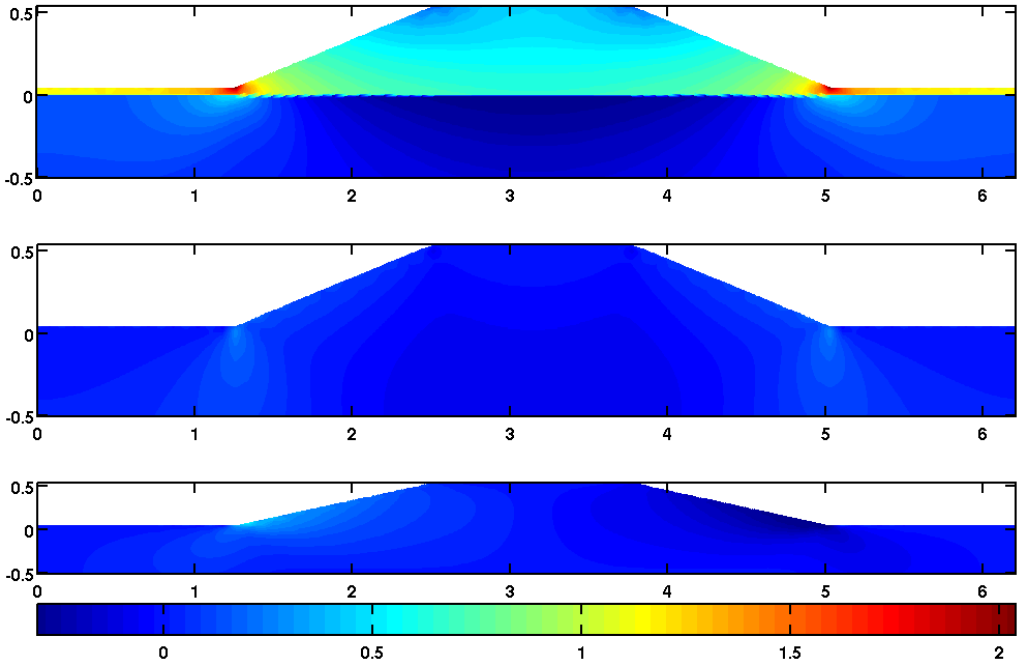

Figure 4.3: Components of stress tensor σ_{xx} (upper), σ_{yy} (middle) and σ_{xy} (lower) inside the T-pyramid quantum dot ($y > 0$) and in the substrate ($y < 0$). Similar dot shape was observed by number of experiments Rastelli et al. (2001); Tersoff et al. (2002).

4.2.2 Linear results with strain energy

Now we add strain energy (which is nonlinear and nonlocal term) to the linear equation from the last section

$$\frac{\partial h}{\partial t} = -\frac{\partial^4 h}{\partial x^4} + \frac{\partial^2 S}{\partial x^2} \quad \text{in} \quad \langle 0, \lambda \rangle \times \langle 0, T \rangle, \tag{4.13}$$

$$\frac{\partial h}{\partial x}(0,t) = \frac{\partial h}{\partial x}(\lambda, t) = 0, \tag{4.14}$$

$$h_0(x) = 1 + 0.01\cos(ax). \tag{4.15}$$

Linear perturbation result of (2.112) with no wetting and isotropic γ gives

$$h(x,t) = e^{\varsigma t}(h_0(x) - 1) + 1, \tag{4.16}$$

where $\varsigma = 4a^3 - a^4$, giving unstable wavenumbers $a < 4$ and fastest growing wavenumber $a = 3$ (corresponding wavelength is $\lambda_1 = \frac{2\pi}{3}$). Comparison of numerical results with initial linear behavior is good and can be seen on Figure 4.4. Perturbation evolves self-similarly and the surface profile remains sinusoidal in the initial stages.

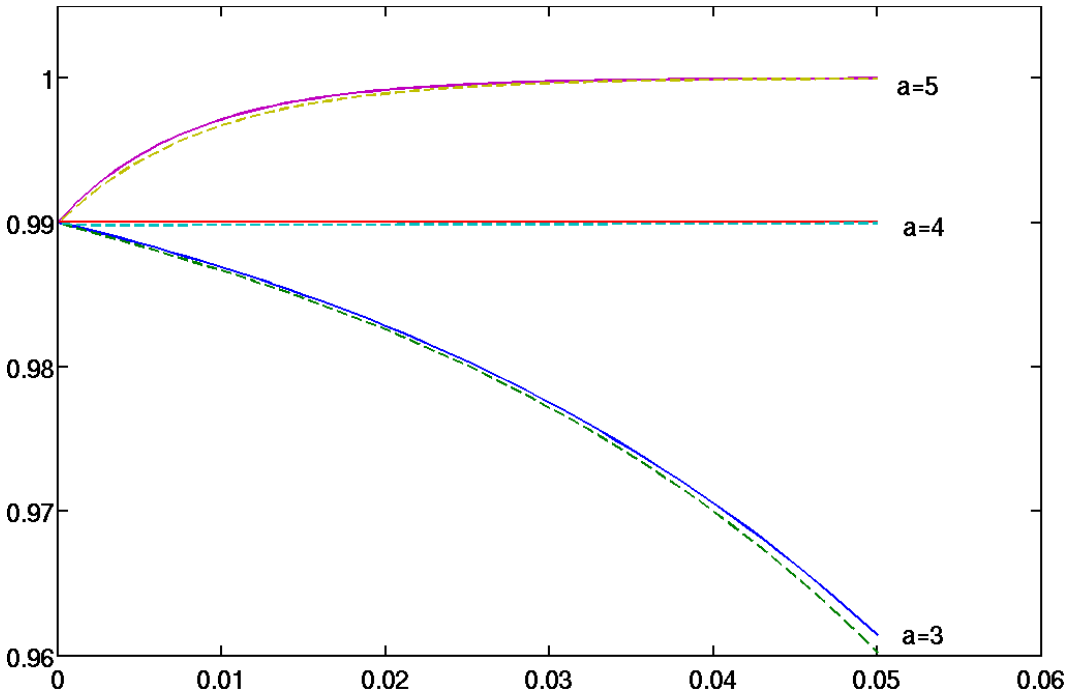

Figure 4.4: Surface evolution at the point $x = \frac{\lambda}{2}$ for $a = 5$ (stable), $a = 4$ (steady) and $a = 3$ (unstable, fastest growing). Data are for uniform space grid with $d = 10^{-2}$ and $T = 0.05$. Solid lines represent initial linear behavior (4.16) and dashed line our numerical approximation.

4.2.3 Nonlinear evolution

Fully nonlinear evolution equation (2.59),(2.60) without wetting and corner regularization is

$$\frac{\partial h}{\partial t} = \frac{\partial}{\partial x}\left[\frac{1}{\sqrt{1+h_x^2}}\frac{\partial(\kappa+S)}{\partial x}\right] \quad \text{in} \quad \langle 0,\lambda\rangle \times \langle 0,T\rangle, \tag{4.17}$$

$$\kappa = -\frac{\partial}{\partial x}\left(\frac{h_x}{\sqrt{1+h_x^2}}\right) \quad \text{in} \quad \langle 0,\lambda\rangle \times \langle 0,T\rangle, \tag{4.18}$$

with periodic boundary conditions and

$$\frac{\partial h}{\partial x}(0,t) = \frac{\partial h}{\partial x}(\lambda,t) = 0, \tag{4.19}$$

$$h_0(x) = 1 + 0.01\cos(ax). \tag{4.20}$$

It was studied first by Spencer and Meiron (1994) and Yang and Srolovitz (1993). The evolution for the fastest growing wavenumber from the linear perturbation analysis $a = 3$ tends to develop cusp in finite time, see Figure 4.5, and we are not able to track the solution numerically after some time. On the other hand, for $a = 3.8$, the evolution develops steady state, see Figure 4.6. Both predictions agree with Spencer and Meiron (1994).

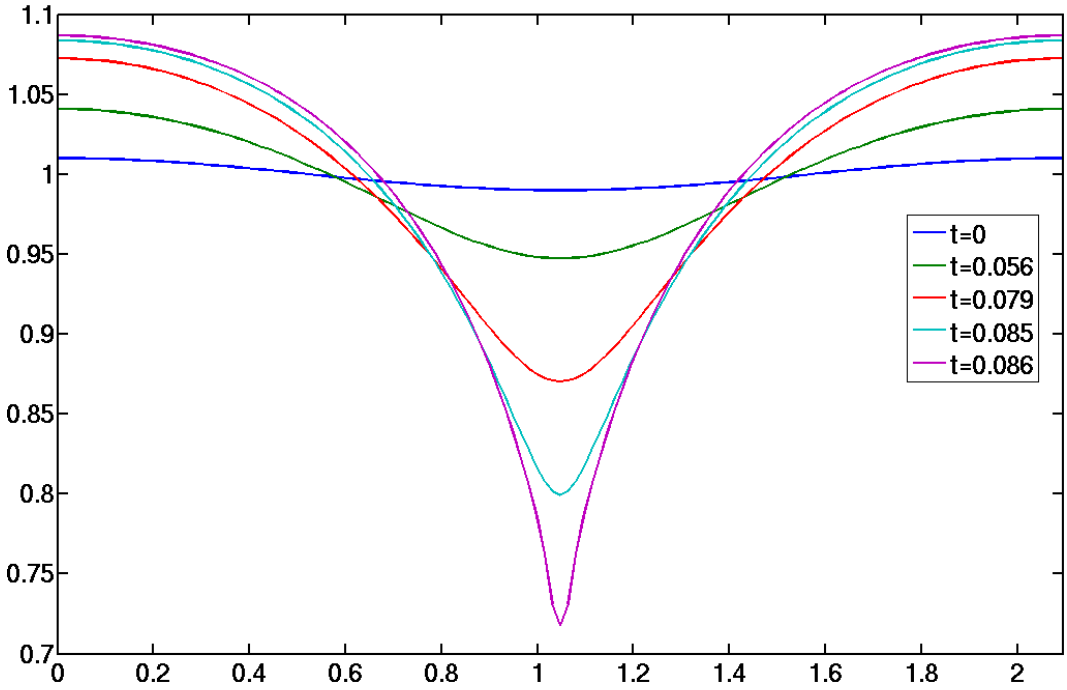

Figure 4.5: Surface evolution for wavenumber $a = 3$ (unstable, fastest growing). Data are for uniform space grid with $N = 128$ and time $T = 0, 0.056, 0.079, 0.085, 0.086$.

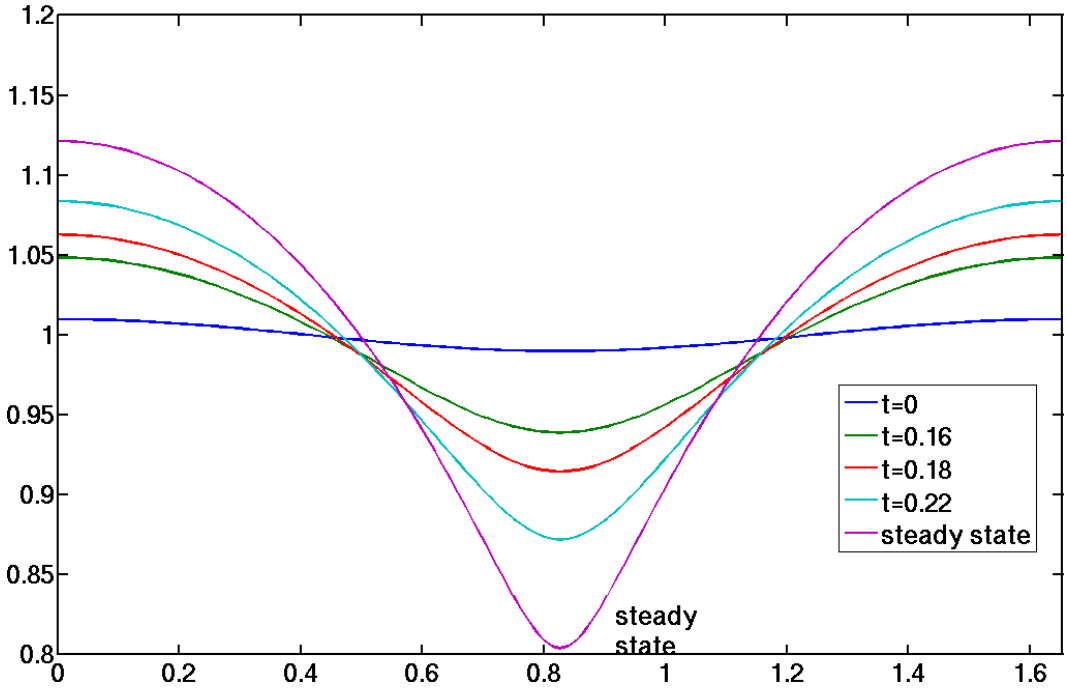

Figure 4.6: Steady state develops for wavenumber $a = 3.8$. Data are for uniform space grid with $N = 128$ and time $T = 0, 0.16, 0.18, 0.22$ and steady state.

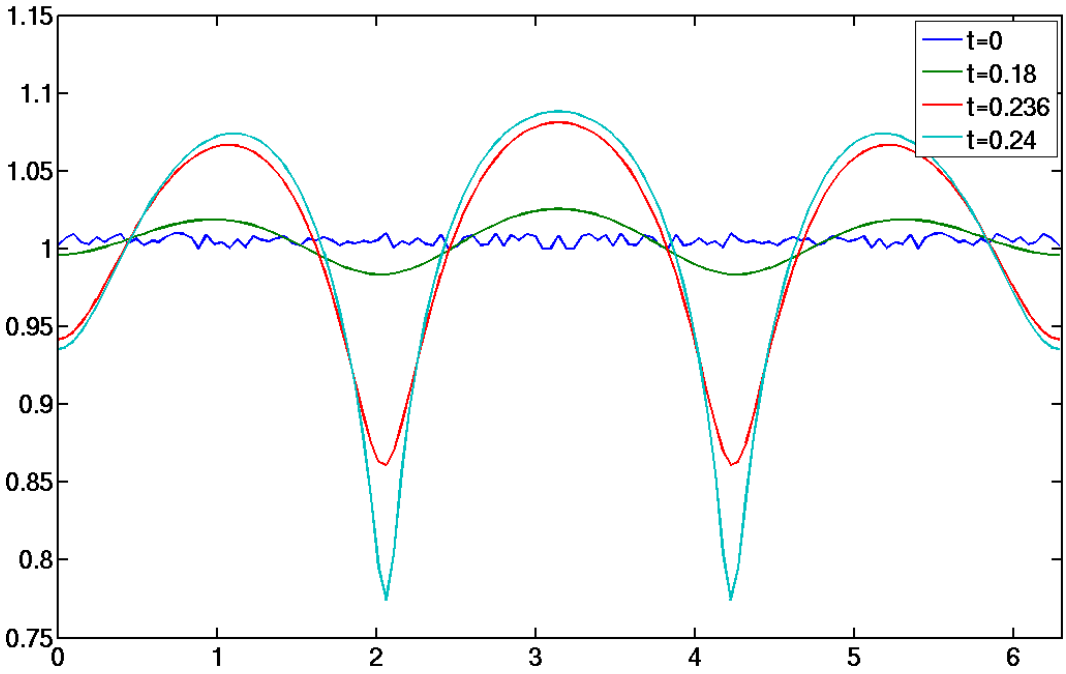

Figure 4.7: Random initial condition with $a = 1$. $N = 128$ and time $T = 0, 0.18, 0.236, 0.24$.

Evolution for a randomly perturbed initial condition

$$h_0(x) = 1 + 0.01 \cdot \mathrm{rand}(x), \tag{4.21}$$

where $\mathrm{rand}(x)$ gives random number in interval $(0, 1)$, confirms predictions of the linear theory. Fastest growing wavenumber $a = 3$ dominates the evolution. We plotted evolution for $a = 1$ on Figure 4.7, as in this case the random initial condition contains all wavenumbers but $a = 3$ develops first.

For $a = 9$ on Figure 4.8, initial condition contains only wavenumbers $a > 3$ that are all damped out, as predicted by the linear theory.

Therefore, it is qualitatively reasonable to simulate the evolution only for the fastest growing wavenumber $a = 3$ in some cases (when properties of single island are studied). Periodic box is chosen to have width of few wavelengths.

4.2.4 Effect of corner regularization

We investigated the influence of corner regularization (2.49) on the evolution (2.60) of islands. No effect was seen for isotropic surface energy from previous test cases for regularization parameter $r = 10^{-3}$ or smaller.

On the other hand, when the corners tend to develop and/or the anisotropy was strong (making the problem ill-posed), omitting the regularization was disastrous and numerical simulation were unstable developing wrinkles.

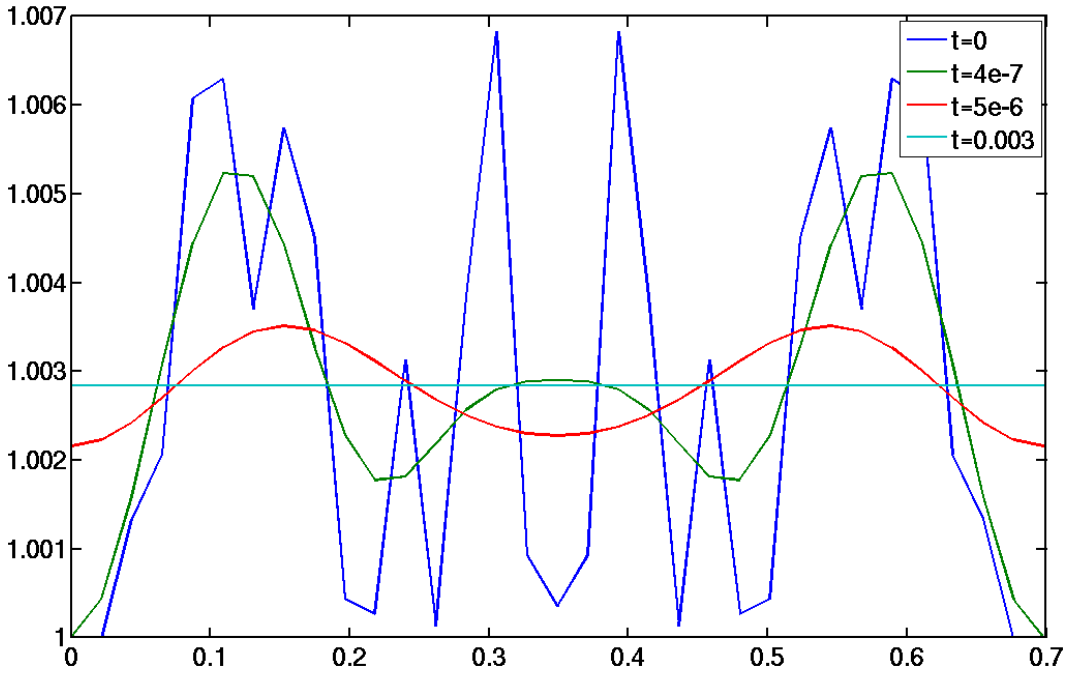

Figure 4.8: Random initial condition and $a = 9$, $N = 32$ and time $T = 0, 4 \cdot 10^{-7}, 5 \cdot 10^{-6}, 0.003$.

4.2.5 Wetting effect

Growth of the cusps in the previous section is prevented by the wetting energy term (2.47) in (2.60), which guarantees that thin wetting layer stays between the growing islands. Films thinner than the critical thickness (2.113) should decay to a planar film according to the linear stability analysis.

In order to make direct comparison with result of Pang and Huang (2006), we choose the same parameters. Films thinner than $h_c = 0.02 \approx 16$ nm or 3 ML (2.113) were seen to decay to a planar film. Evolution for initial height $h_0 = 0.025$ above the critical thickness is plotted on Figure 4.9. At the initial stages, fastest growing wavenumber develops first, but the growth slows down once it comes near the film/substrate interface ($t = 1.1$). Coarsening starts afterwards, when the middle island grows at the expense of those at the sides, reminding the decreasing island density seen in experiment Ross et al. (1998). This process seams to stop and steady state morphology is reached numerically ($t = 20$) and is stable against subsequent coarsening ($t < 500$), because no more material can be diffused. Substrate stays covered with thinner inter island wetting layer (thickness 0.01 or 1-2 ML, it is entirely determined by the transition thickness parameter b) which cannot be removed from energetical reasons. The trough at the island sides is common for all simulations. This is consistent with the results of Tekalign and Spencer (2004), Pang and Huang (2006), Eisenberg and Kandel (2005).

Simulation results for random perturbated initial conditions can be seen on Figure 4.10 ($a = 0.5$). Fastest growing wavenumber $a = 3$ is seen to

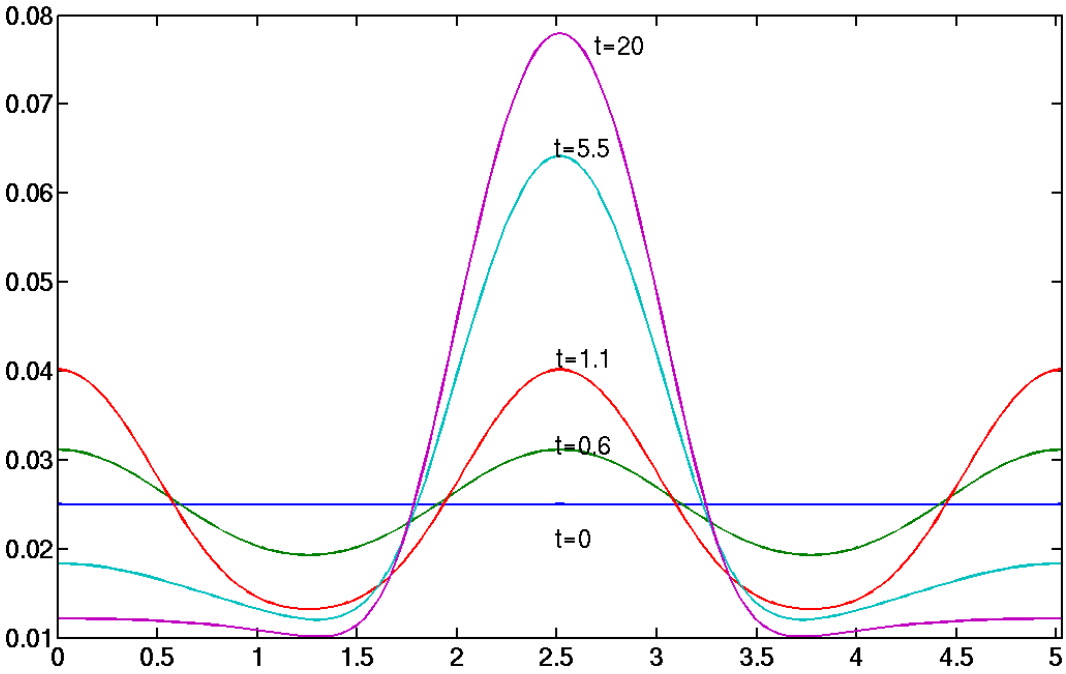

Figure 4.9: Evolution with wetting energy for initial conditions of Pang and Huang (2006) $h_0(x) = 0.025 + 2.5 \cdot 10^{-5} \cos(ax)$ and $a = 1.25$, $N = 128$, $b = 2.5 \cdot 10^{-4}$. Be aware of different scalings used by Pang and Huang (2006), $4L = l_0$ and $256\tau = \tau_0$.

really develop first and then ripening occurs, some islands dissapear and just one big island remains as in Eisenberg and Kandel (2005) (Fig.8). On the contrary, we did not observe the steady morphology computed in this work for $h_c < h < h_c + 1ML$ (qualitatively same results as in Figure 4.10 were obtained). This could be caused by different mechanism for wetting which included nonlinear elastic free energy in their work.

We have tried the simulations with their term

$$\frac{\mathrm{d}f_{el}^{(0)}}{\mathrm{d}h}(h) = S_0(1 - 0.05\exp(-\frac{h}{h_{ML}})) \quad \text{for} \quad h > 0, \tag{4.22}$$

and zero for $h \leq 0$ with $h_{ML} = 0.1$. This was included in the chemical potential (2.54) insted of our wetting term (2.47), but the numerical evolution had problems with abrupt change in behavior of $\frac{\mathrm{d}f_{el}^{(0)}}{\mathrm{d}h}(h)$ and this produced instability at the film/substrate interface. In fact, Eisenberg and Kandel (2002) also reported some numerical instability by directly computing the chemical potential this way and used more physical approach based on the material movement on the surface together with some tricks to keep the inter island wetting layer on the substrate.

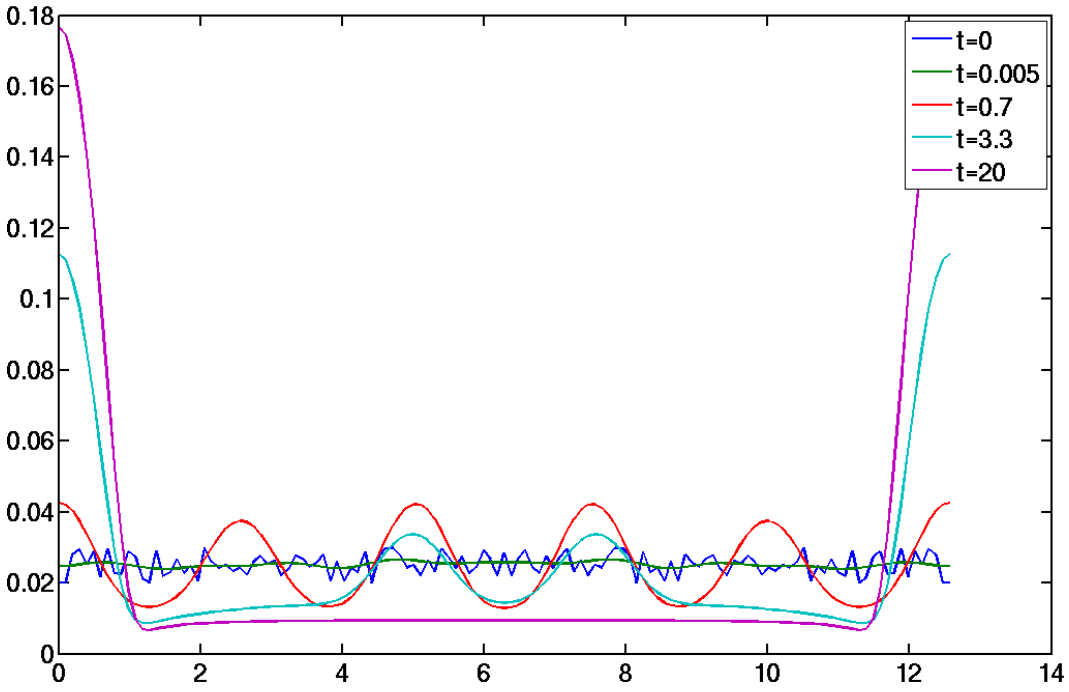

Figure 4.10: Evolution with wetting energy for initial condition $h_0(x) = 0.025 + 0.01 \cdot \mathrm{rand}(ax)$ and $a = 0.5$, $N = 128$, $b = 2.5 \cdot 10^{-4}$.

4.2.6 Deposition effects

So far, deposition flux was assumed zero and annealing of thin films was studied exclusively. In this section we solve evolution equation (2.60) with constant deposition rate v_d for two methods of deposition - MBE (2.1) and LPE (2.2).

Comparison with results of Eisenberg and Kandel (2002) for isotropic surface energy, $a = 3$ and high deposition rate $v_d = 250$ is on Figures 4.11 and 4.12. Cusp formation is seen for MBE, since the deposition affects the evolution only by enlarging the surface height. On the other hand, steady morphology (preserving shape) is reached for LPE, because the material is deposited faster on the cusps and thus slows down its formation.

Different outcome is produced for wavenumber $a = 3.8$, Figures 4.13 and 4.14. Both methods of deposition lead to the steady morphology and similar to the steady states seen in infinitely thick film by Spencer and Meiron (1994). This is in agreement with results of Chiu and Gao (1995), who showed that different morphologies can be obtained for different values of ratio v_d/a^2 during LPE deposition. Cusps are produced for $v_d/a^2 \approx 1$, steady state morphologies for $v_d/a^2 \gg 1$.

General random large sample was studied on Figure 4.15 with constant MBE deposition rate $v_d = 0.1$. Initially surface grows mainly flat, but as the fastest growing wavelength develops, islands are formed and then they grow only vertically. If the deposition is stopped, they seem to be metastable during short term annealing.

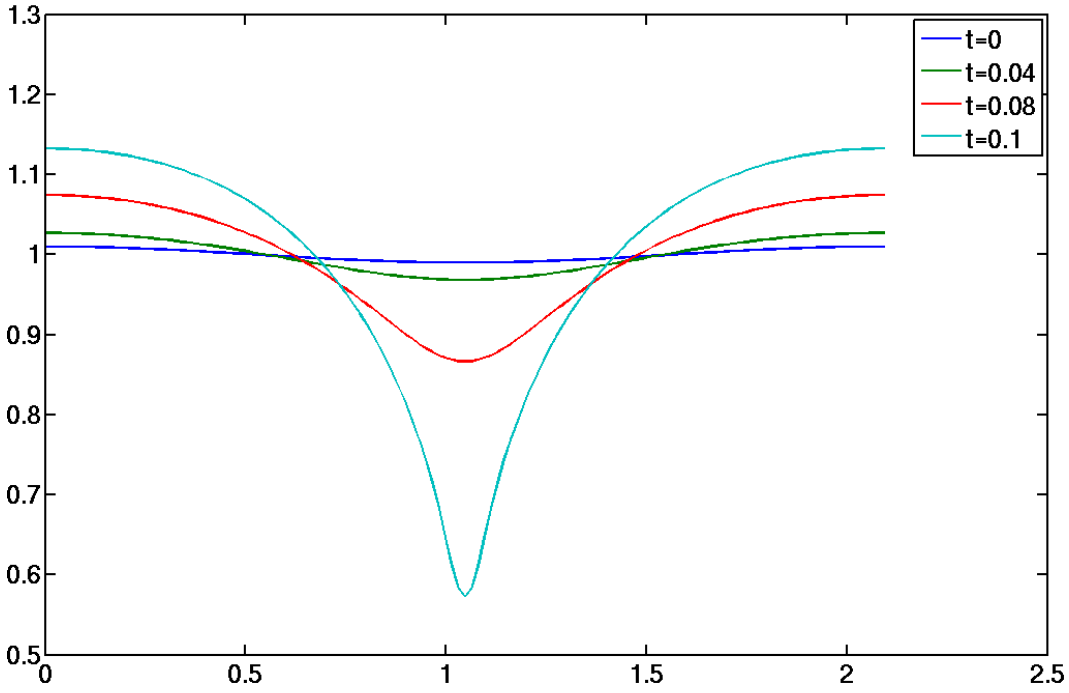

Figure 4.11: Cusp formation in MBE deposition, very high deposition rate $v_d = 250$ and $a = 3$. Value of $h - v_d t$ instead of h is plotted to keep the same scale.

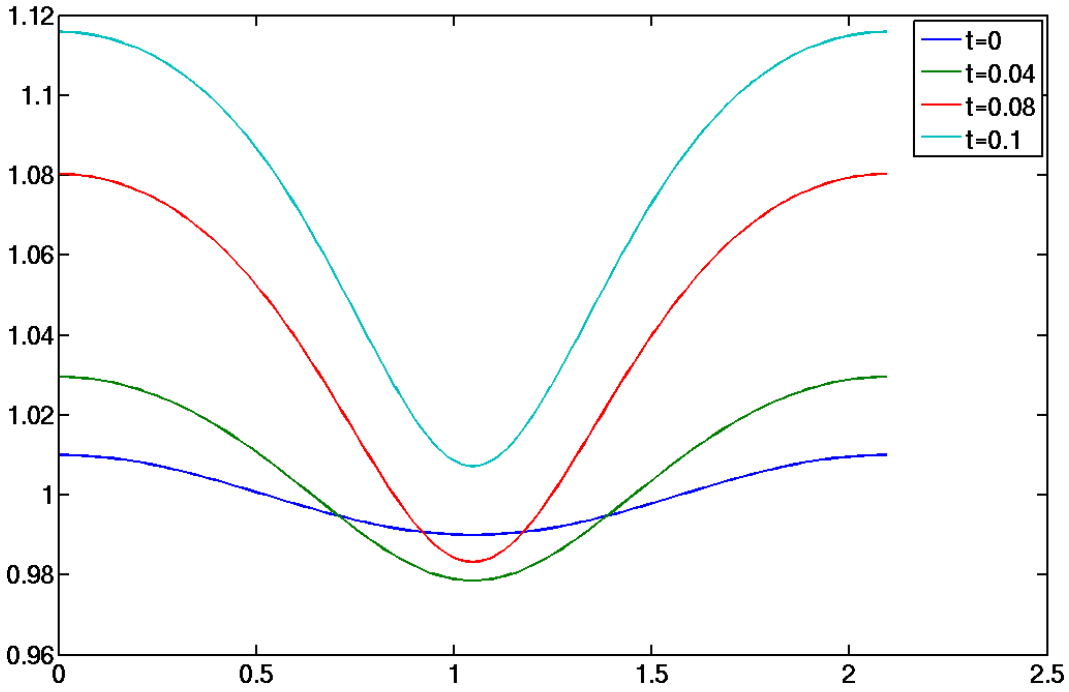

Figure 4.12: Steady state for LPE deposition, very high deposition rate $v_d = 250$ and $a = 3$. Value of $h - v_d t$ instead of h is plotted to keep the same scale.

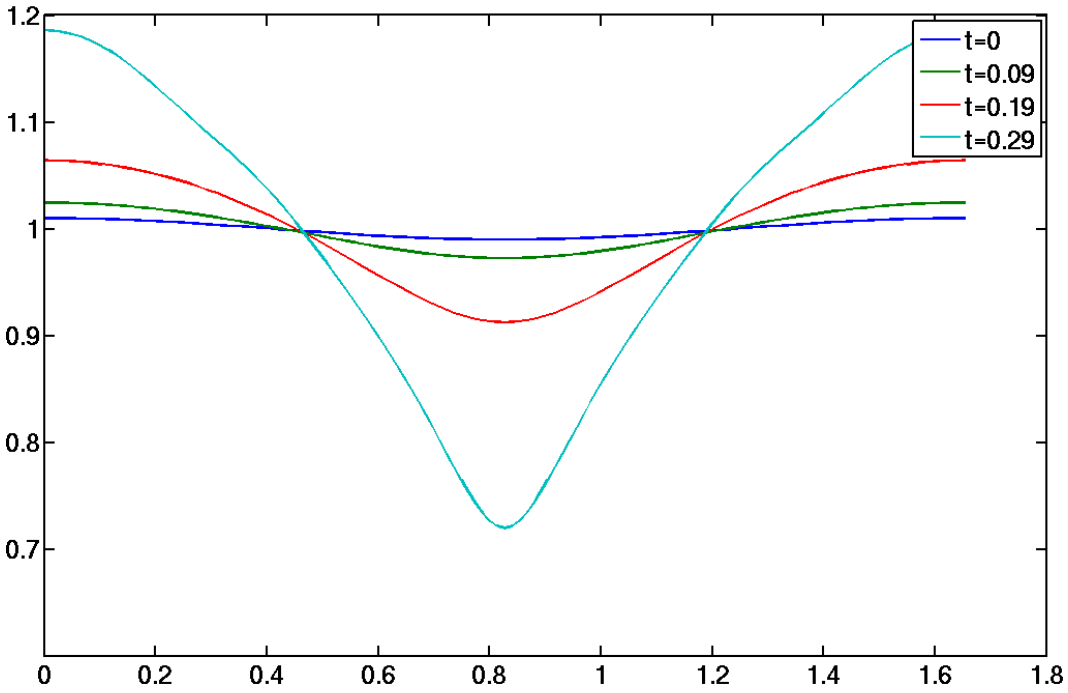

Figure 4.13: Steady state for MBE deposition, very high deposition rate $v_d = 250$ and $a = 3.8$. Value of $h - v_d t$ instead of h is plotted to keep the same scale.

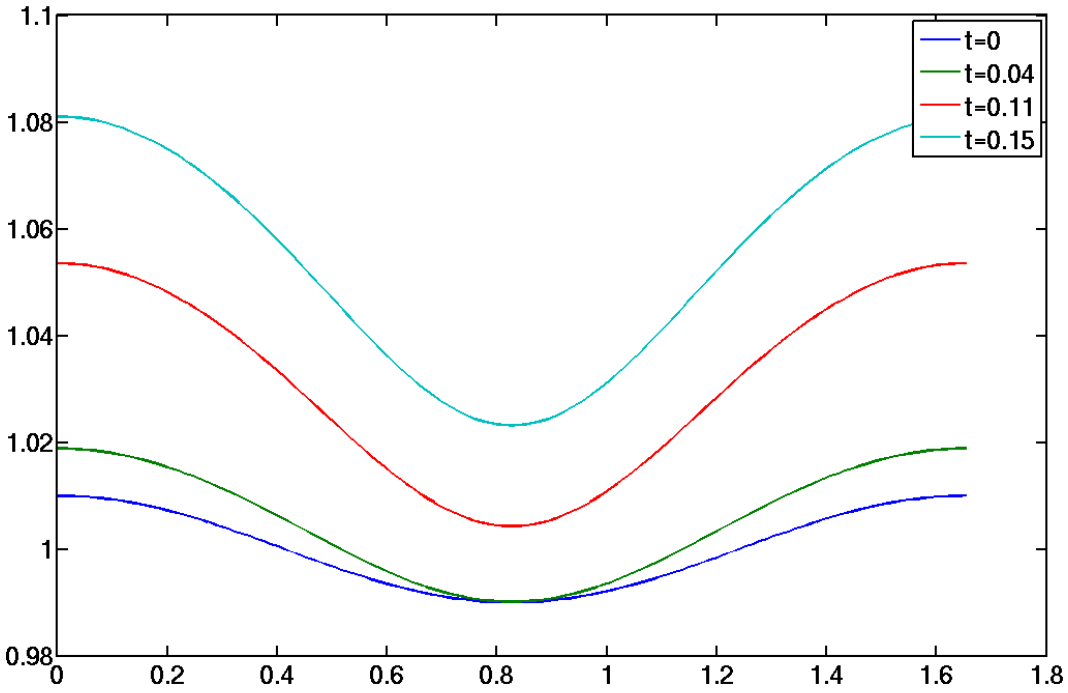

Figure 4.14: Steady state morphology for LPE deposition, very high deposition rate $v_d = 250$ and $a = 3.8$. Value of $h - v_d t$ instead of h is plotted to keep the same scale.

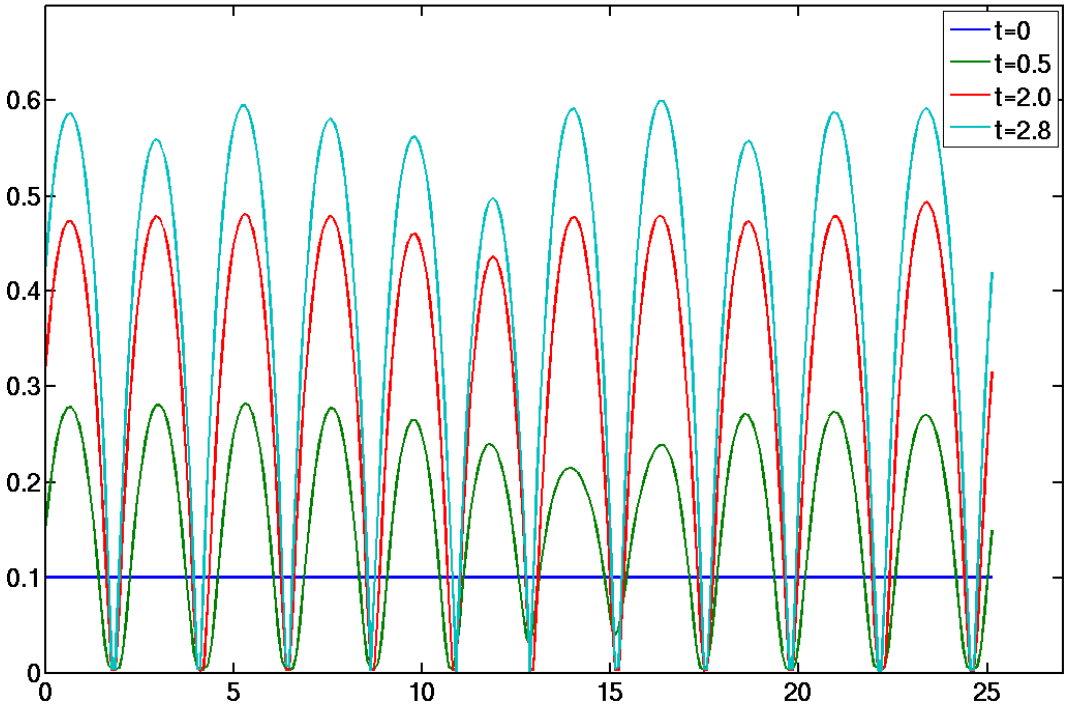

Figure 4.15: Evolution with MBE deposition $v_d = 0.1$ and $\Upsilon_1 = 1, h_f = 0.1, a = 0.25$, $N = 256$, $b = 2.5 \cdot 10^{-4}$.

4.3 Smooth anisotropic surface energy

Above the roughening temperature, crystalline materials exhibit smoothly anisotropic or isotropic surface energy. We will study the impact of the surface energy γ_2 for different facet angles.

4.3.1 Facets at 45 degrees

Parameters used by Long et al. (2001) $g = 0.05, \beta = 4$ for γ_2 lead to surface stiffness Υ_2 that becomes negative for certain angles, making the problem ill-posed. In their numerical formulation no surface stiffness was calculated and it appeared naturally from the algorithm used. This was seen in our evolution study as blow-up at all length scales Spencer (2004) and corner regularization (2.49) was needed. This regularizing term smoothes the small-scale instability and removes the ill-posedness. This result can be seen in Figure 4.16, without any qualitative difference for smaller regularization parameter r. Two faceted islands develop at the distance ≈ 6 and they ripen until all material is consumed. This island spacing corresponds well with the fastest predicted growth wavelength (2.116), $\lambda_2 \approx 5.5$. We have not observed the triangular shapes (with facet angle 30°) reported by Long et al. (2001) and our results show T-pyramid quasiequilibrium shapes (notation corresponds to Rastelli et al. (2001)), Figure 4.17. This is awarded by Gill to the different variational formulation (using not surface stiffness in the formulation) and its weakness to

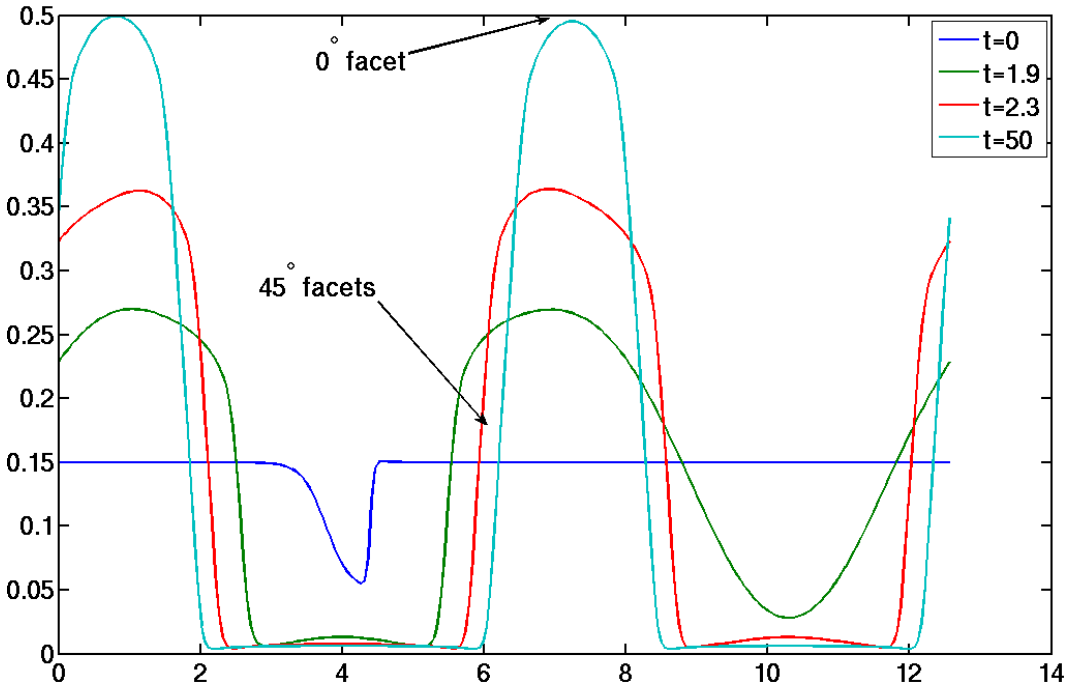

Figure 4.16: Evolution with Υ_2 ($g = 0.05, \beta = 4$) for perturbed initial condition $h_f = 0.15$ and $a = 0.5$, $N = 256$, $b = 2.5{\cdot}10^{-4}, r = 10^{-3}$. Facets have developed at 45° and 0°.

enforce 0° facet at the top of the triangle.

The influence of the strength of anisotropy on the quasiequilibrium shape is on Figure 4.17. Facets are more sharp for $g = 0.05$, as the surface stiffness is negative for orientations around the facet and therefore this high energy angles are prohibited. For $g = 0.02$ there is no negative surface stiffness and facets meet not so sharply because the orientations near facet are possible.

Larger samples were studied to study the effect of coarsening, Figure 4.18. Number of small islands have developed next to the perturbation ($t = 2.7$), smaller dissapear ($t = 6.7$) and this process continues over longer length scale ($t = 50 - 200$), because islands influence each other slowly when their distance is increasing.

Evolution during MBE with deposition of $v_d = 0.1$ leads to the formation of nice regular array of nearly equally sized islands, Figure 4.19. The coarsening process, which is just the surface diffusion of atoms between different islands, is suppressed by the deposition from above and the atoms have little time to diffuse along the surface. If the deposition is stopped and sample is further annealed, it shows signs of metastable morphology that will not coarsen into smaller number of bigger islands.

4.3.2 Facets at 11 degrees

We have done comparison with equilibrium island shapes obtained by Tersoff et al. (2002) with the same parameters used there (11,22° facets with $\gamma_{\mathrm{Te}}, \beta =$

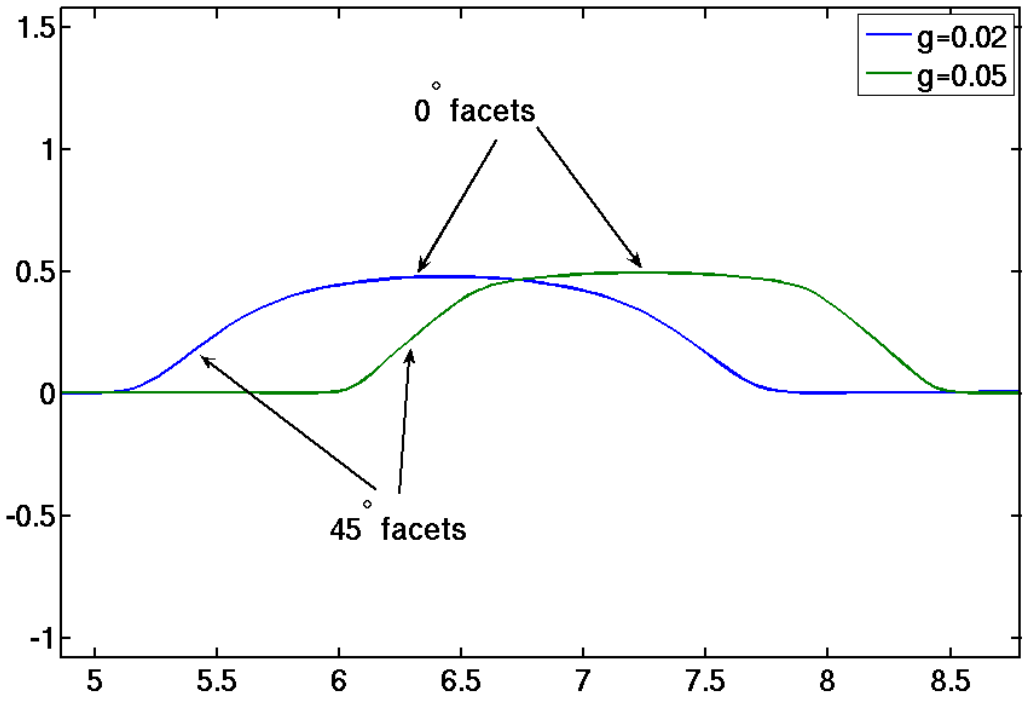

Figure 4.17: Quasiequilibrium shapes of T-pyramids - sharper corners for $g = 0.05$ and smoother for $g = 0.02$.

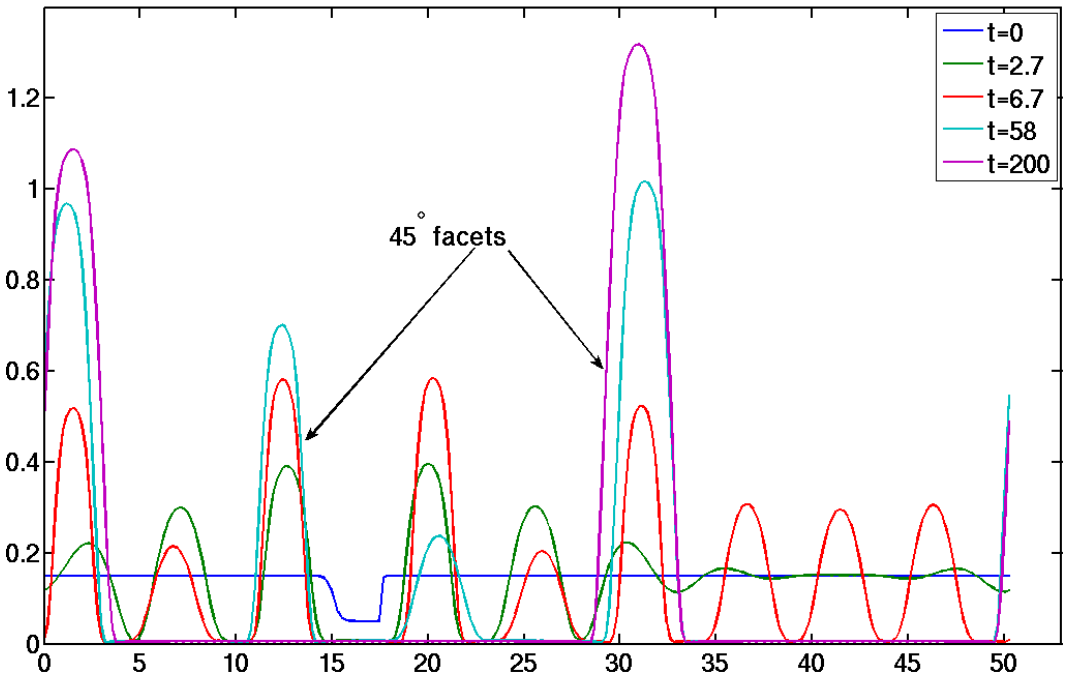

Figure 4.18: Evolution with Υ_2 ($g = 0.05, \beta = 4$) for perturbed initial condition $h_f = 0.15$ and $a = 0.125$, $N = 256$, $b = 2.5 \cdot 10^{-4}, r = 10^{-3}$.

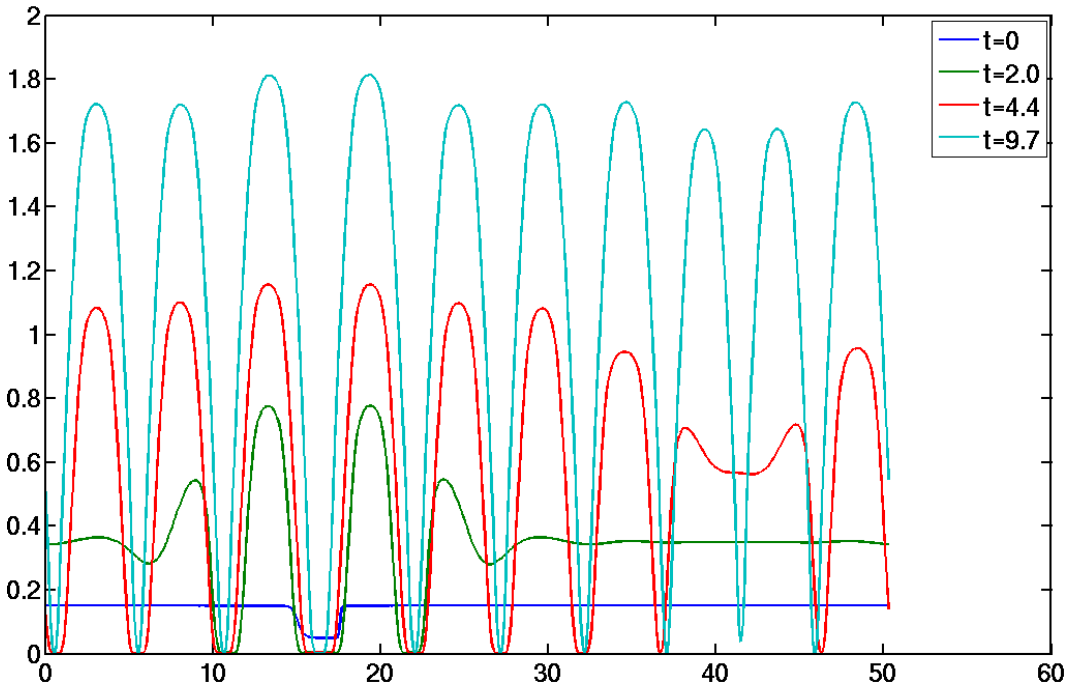

Figure 4.19: Evolution of regular island array with Υ_2 ($g = 0.05, \beta = 4$) for perturbed initial condition $h_f = 0.15$ and $a = 0.125$, $N = 512$, $b = 2.5 \cdot 10^{-4}, r = 10^{-3}$.

$32, g = 0.0015$) converted to our scalings. We have enforced the very small wetting layer by taking $b = 10^{-11}$ which makes the critical thickness of the linearly stable wetting layer $h_c = 10^{-4}$. Results of our evolution calculations are on Figure 4.20. At small volumes only cosinelike shapes are possible, but for greater volumes faceted islands develop. Even larger islands have "dome" shape with higher facet orientations $\pm 22°$, what will be later described as pyramid to dome shape transition. Island edges meet the substrate at zero contact angle. Phase transition from prepyramids (cosinelike shapes) to pyramids (faceted islands) is completely described in their work and compared to the experimental data from STM.

Essentially the same minima can be obtained with $\gamma_2, \beta = 16, g = 0.0015$ as with $\gamma_{\mathrm{Te}}, \beta = 32, g = 0.0015$. We studied the long time evolution of large samples in this case, Figure 4.21. Lowest angle facet 11° develops first on the islands and during coarsening small islands dissapear and bigger acquire higher facet angles 22° and 33°.

4.4 Cusped anisotropic surface energy

Evolution equation (2.60) will be solved with cusped surface energy γ_3, γ_4 or Υ_3, Υ_4 respectively. Linear stability analysis for cusped anisotropic case γ_3 without wetting differs significantly from the case when smooth surface energy was assumed. It was done by Long et al. (2001), Gill with the essential result

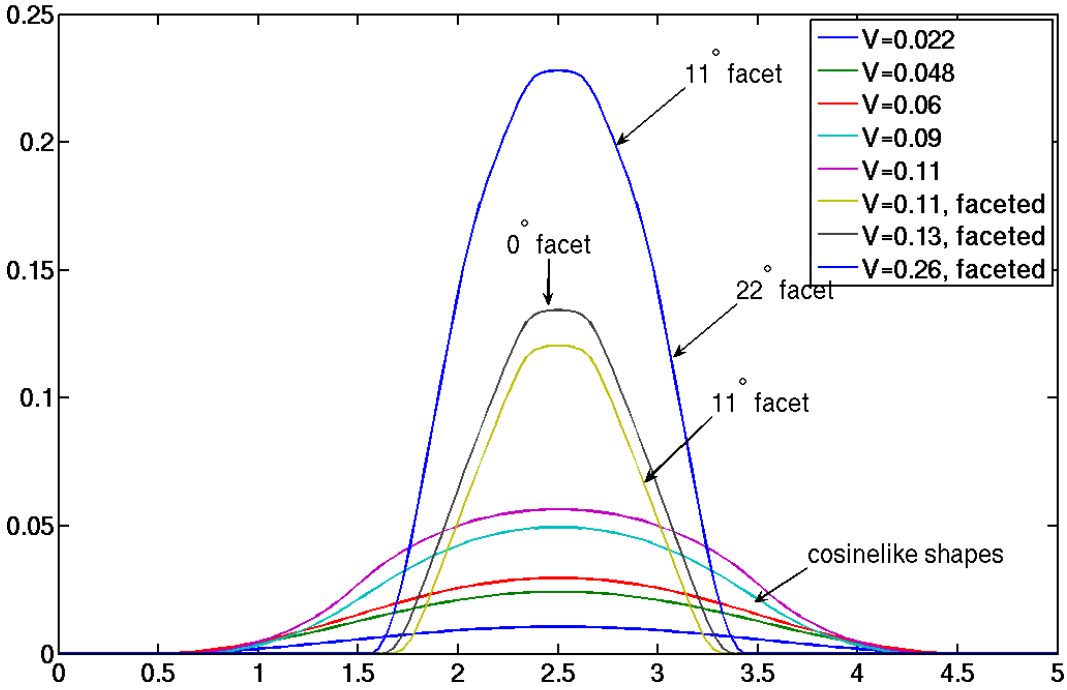

Figure 4.20: Equilibrium island shapes for different island volumes, parameters were taken from Tersoff et al. (2002), $\gamma_{\mathrm{Te}}, g = 0.0015, \beta = 32$.

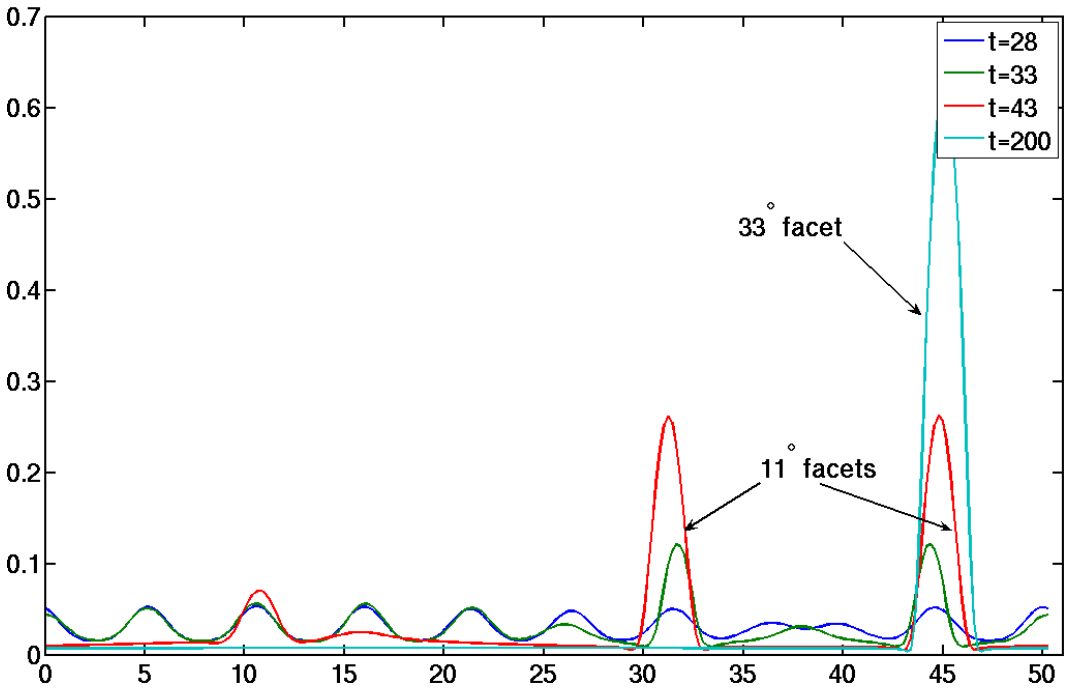

Figure 4.21: Number of small islands have developed ($t = 28$) and then bigger grow at the expense of smaller ($t = 33, 43$). Finally just one big island remains. Υ_2 ($g = 0.0015, \beta = 16$), $h_f = 0.03$ and $a = 0.125$, $N = 256$, $b = 2.5 \cdot 10^{-4}, r = 10^{-3}$.

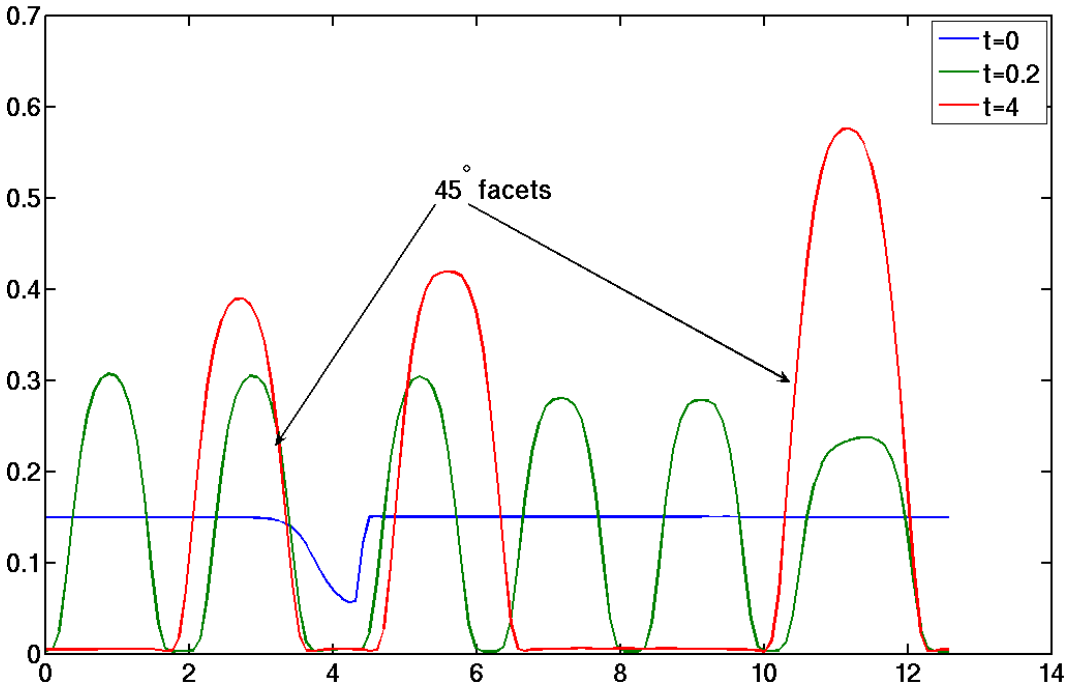

Figure 4.22: Annealing of disturbed flat film $h_f = 0.15$ with $a = 0.5, N = 128$ and $\Upsilon_4, g = 0.05, \beta = 4, G = 500$.

that the perturbation amplitude must be above critical value

$$p_0 > \frac{\beta g}{\pi} \tag{4.23}$$

in order to destabilize the film. Fastest growing wavenumber in this case is

$$a_3 = 4\left(1 - \frac{\beta g}{\pi p_0}\right). \tag{4.24}$$

As pointed out first by Long et al. (2001), this result is very different from the result of linear stability for γ_4, which gives no dependence on the perturbation amplitude and predicts stable film for $G \to \infty$. This result is valid for weak anisotropy with the amplitude to wavelength ratio of roughly 0.05 or less, so we are at its limit in our case where $\frac{\beta g}{\pi} \approx 0.06$. Therefore, and also according to the nonlinear analysis of a large perturbation model by Gill, smaller amplitude perturbations than p_0 could be unstable.

When we used Υ_4 in numerics, Figure 4.22, the computations were rather slow because of the blow-up in the graph of Υ_4 at $\beta\theta = n\pi$, which introduces difficulties in the numerical scheme (timestep is very small for desired accuracy). Computations with $G = 50$ were faster, but not as much as with Υ_3. **Interestingly, when we used the surface stiffness Υ_3 (without blow-ups, see Figure 2.6), no qualitative change was seen and computations were many times faster. Most results henceforth were computed using Υ_3.** It is clear that blow-up in Υ_4 can substantially stabilize facet orientations during evolution, much more than Υ_3, as was shown by Eisenberg and Kandel (2005).

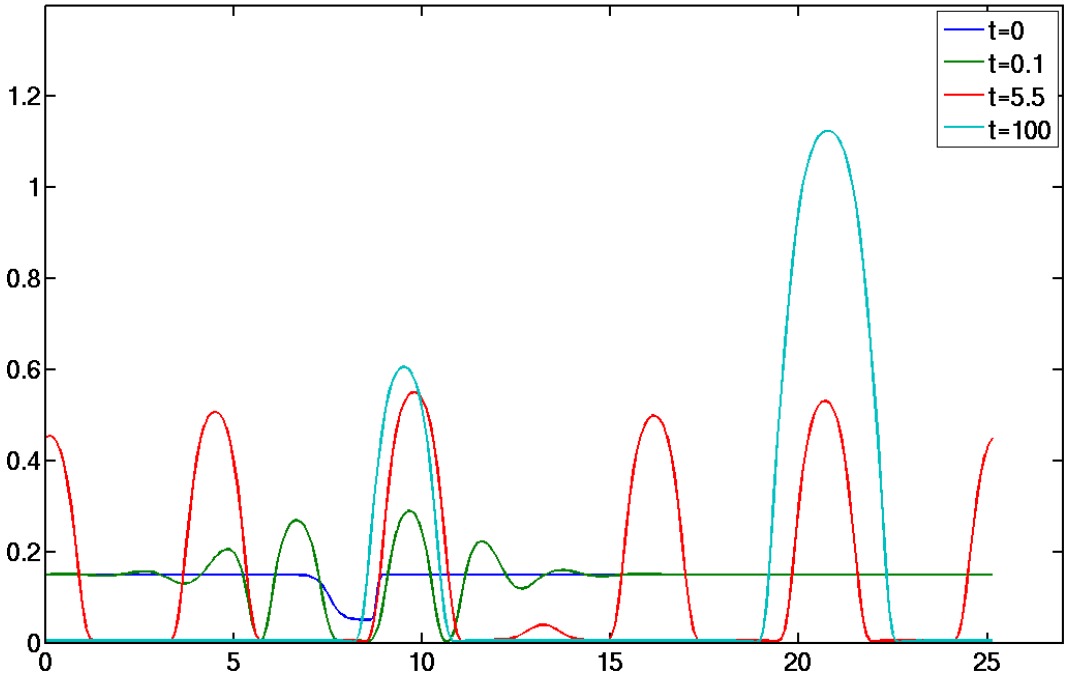

Figure 4.23: Annealing of disturbed flat film $h_f = 0.15$ with $a = 0.25$, $N = 256$ and $\Upsilon_3, g = 0.05, \beta = 4$.

4.4.1 Facets at 45 degrees

We calculated the evolution for $g = 0.05, \beta = 4$ to make qualitative comparison with the results of Eisenberg and Kandel (2005). First we tried the evolution equation (2.60) without the regularization term (2.49) but it was unstable after the creation of edges. After we have included this term in the equation (Figure 4.23), we could compute the evolution for any time limited only by the computational demands. Neighboring islands grow next to the perturbation ($t = 0.1, 5.5$), which undergo long time coarsening ($t = 100$).

This is in agreement with number of experimental observations Mo et al. (1990); Medeiros-Ribeiro et al. (1998); Kamins et al. (1997); Moison et al. (1994) and simulation studies Long et al. (2001); Eisenberg and Kandel (2005), where the islands maintain fixed height-diameter ratio (shape) as they grow. Inter island wetting layer of thickness about $5 \cdot 10^{-3}$ (1 ML) (for $b = 2.5 \cdot 10^{-4}$) stays at the substrate consistent with observations of Moison et al. (1994); Ozkan et al. (1997) and cannot be removed. Larger value of b produces larger wetting layer.

As experimentally observed by Tromp et al. (2000) and others, new islands are developing near other islands ("chain-reaction ripple effect"), because the growth destabilizes the flat faceted film at island boundaries. This can be also seen on Figure 4.23.

Quasiequilibrium island is shown in correct aspect ratio on Figure 4.24, where $0°, 45°$ facets can be roughly seen. Since our continuum model and corner regularization are smoothing the edges, they are not perfect in the

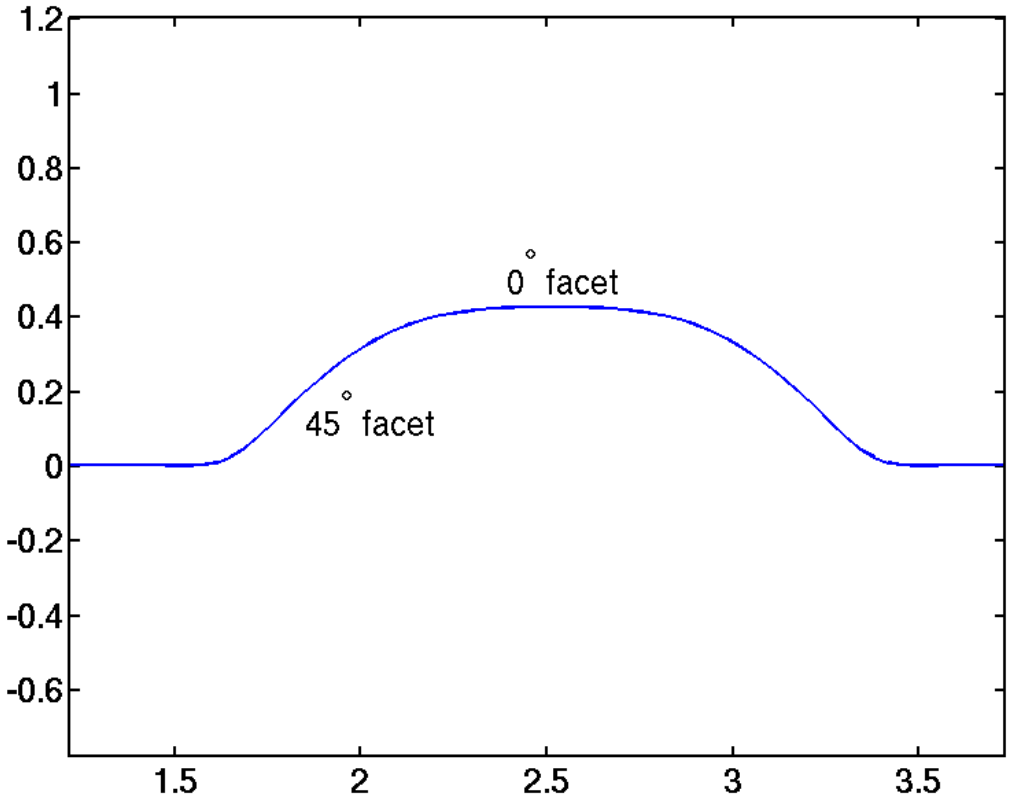

Figure 4.24: Metastable island in 1:1 aspect ratio, $\Upsilon_3, g = 0.05, \beta = 4$.

angle nor in the corners.

Few islands were studied during MBE deposition to see the shape transition between pyramid and dome, Figures 4.25, 4.26. We see islands growing preserving their aspect ratio in the beginning (pyramids). After some critical width, their sides exceed 45° angle and they grow only vertically (domes). This effect can be already seen for smoothly anisotropic surface energy on Figure 4.20, it is not constrained just to the cusped surface energy. This well corresponds to the experimental observations in Section 1.3.

Constant deposition rate $v_d = 0.1$ was assumed during MBE, Figure 4.27. Initially film grows just vertically but small undulations soon develop and some parts reach the substrate. From this moment, quite regular array of islands grows vertically, eventually changing shape, what can be not seen in this graph. If the deposition is stopped here and sample is annealed, it is metastable and this could be used to produce stable regular positioned island array.

4.4.2 Facets at 11 degrees

Similar qualitative behavior as in the smooth case was obtained for Υ_3 and surface energy minima at $0, \pm 11°, \pm 22°$, Figure 4.28. Number of small islands appear ($t = 4, 7$) and then bigger grow at the expense of smaller over longer length scale ($t = 50, 200$).

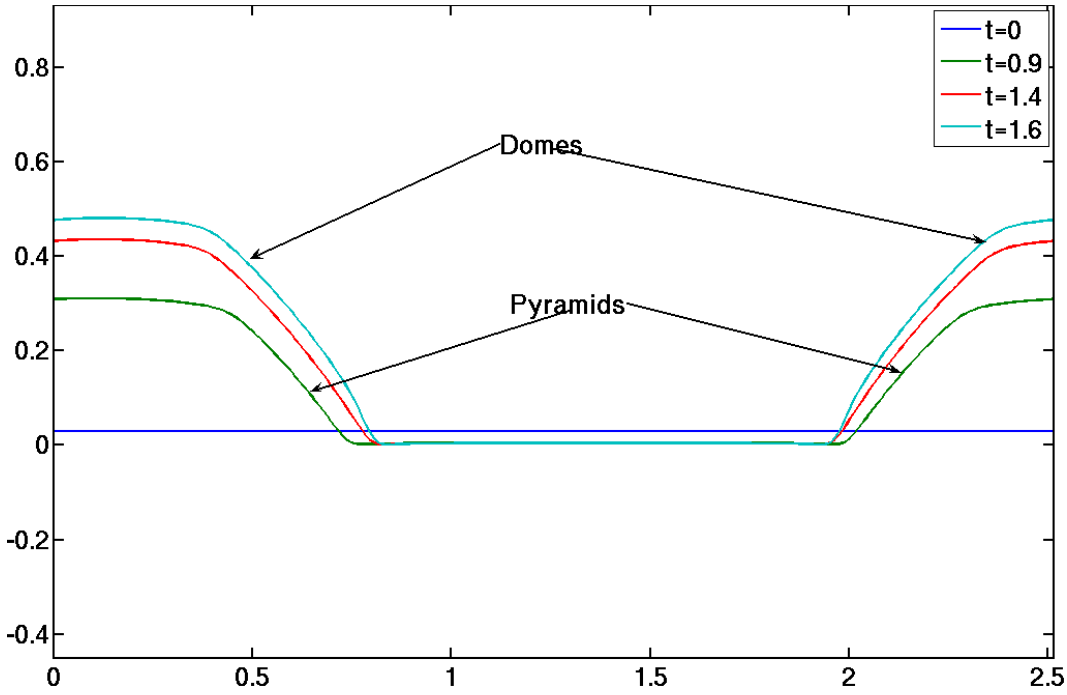

Figure 4.25: Increasing the size, pyramid aspect ratio remains roughly the same ($t = 0.9, 1.4$). When the dome is introduced ($t = 1.6$), it grows only vertically. Parameters $v_d = 0.1$, $\Upsilon_3, g = 0.07, \beta = 4$.

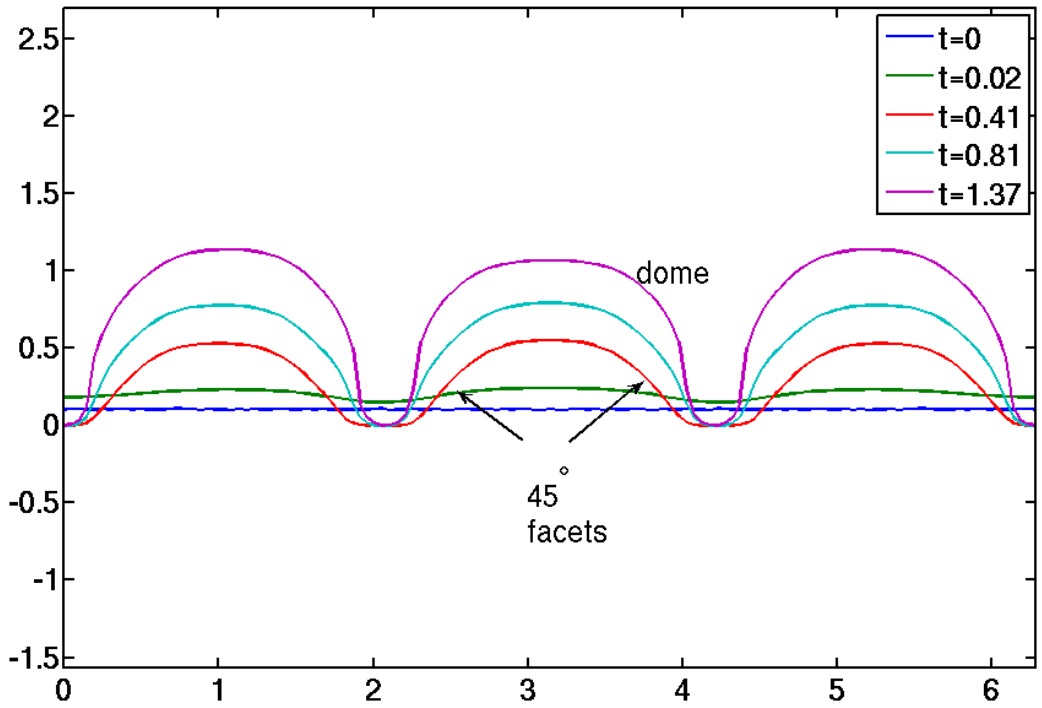

Figure 4.26: Pyramid-to-dome transition during MBE growth with deposition rate $v_d = 0.5$. $\Upsilon_3, g = 0.05, \beta = 4$.

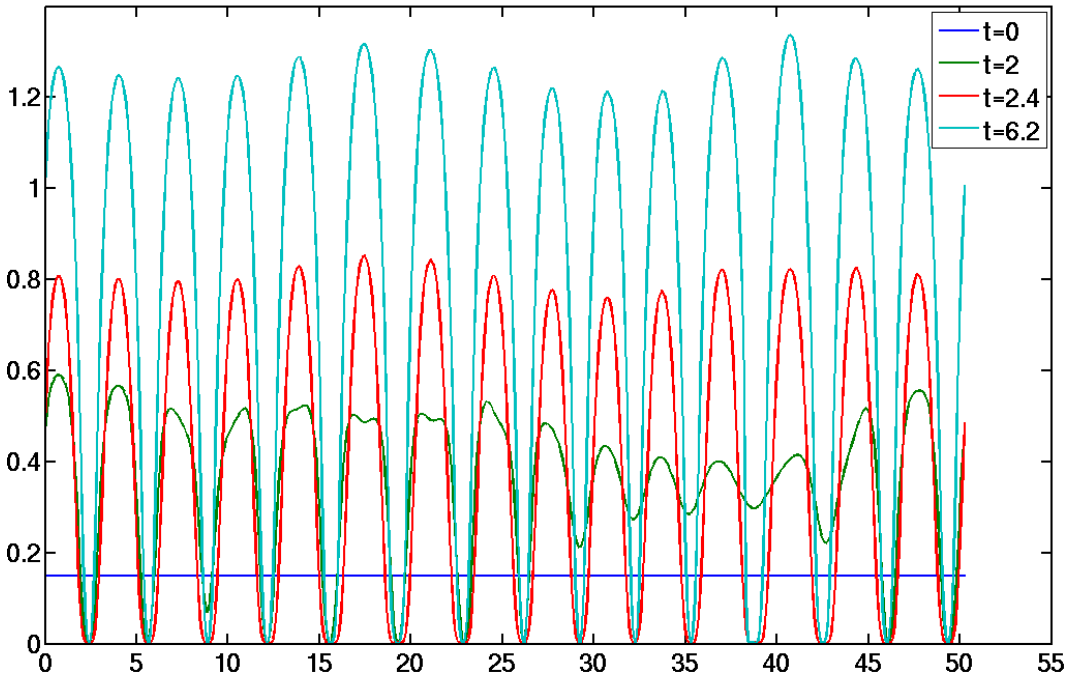

Figure 4.27: Deposition $v_d = 0.1$ on a disturbed flat film $h_f = 0.15$ with $a = 0.125, N = 512$ and $\Upsilon_3, g = 0.07, \beta = 4$.

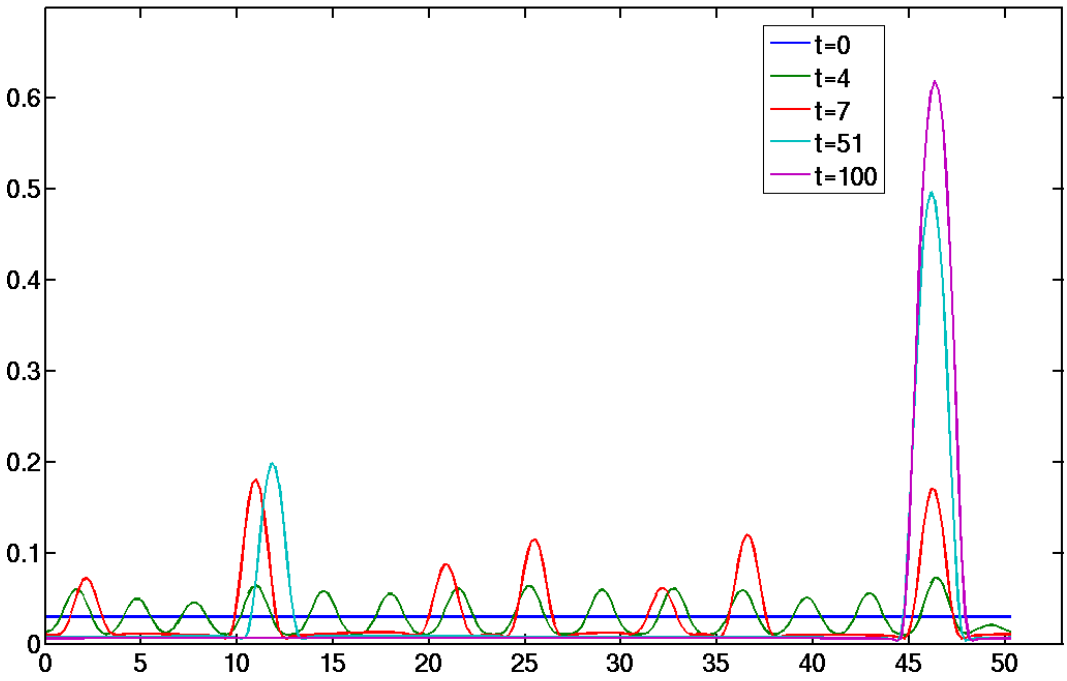

Figure 4.28: Coarsening for weak Υ_3 ($g = 0.0015, \beta = 16$), $h_f = 0.03, a = 0.125, N = 256$, $b = 2.5 \cdot 10^{-4}, r = 10^{-3}$.

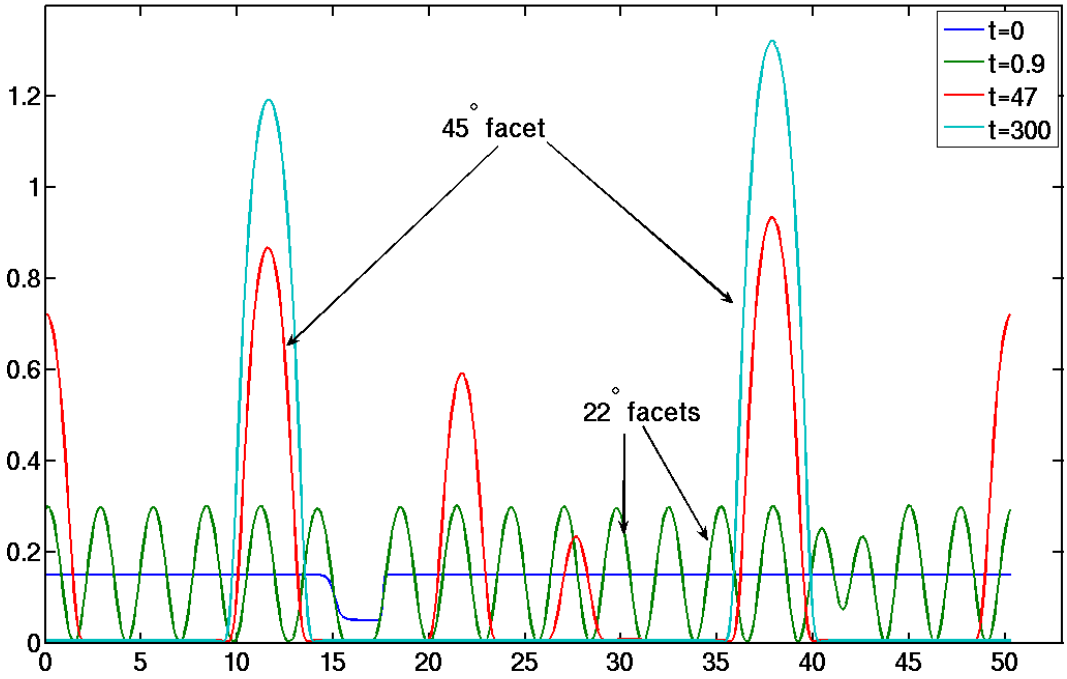

Figure 4.29: Evolution of higher sample, Υ_3 ($g = 0.0015, \beta = 16$), $h_f = 0.15, a = 0.125, N = 512$, $b = 2.5 \cdot 10^{-4}, r = 10^{-3}$.

When higher sample is annealed (and thus more material can diffuse to make islands), Figure 4.29, small islands grow more dense together ($t = 0.9$) and decay into bigger islands just over long time ($t = 40 - 300$), indicating their meta-stability. As already mentioned, the stability is in reality enhanced by bigger stiffness maxima at the facet orientations.

Evolution with constant deposition rate $v_d = 0.1$ was calculated during MBE, Figure 4.30. Quite regular array of islands develops ($t = 1.6$) and from this moment, they grow only vertically. If the deposition is stopped, they are metastable against ripening.

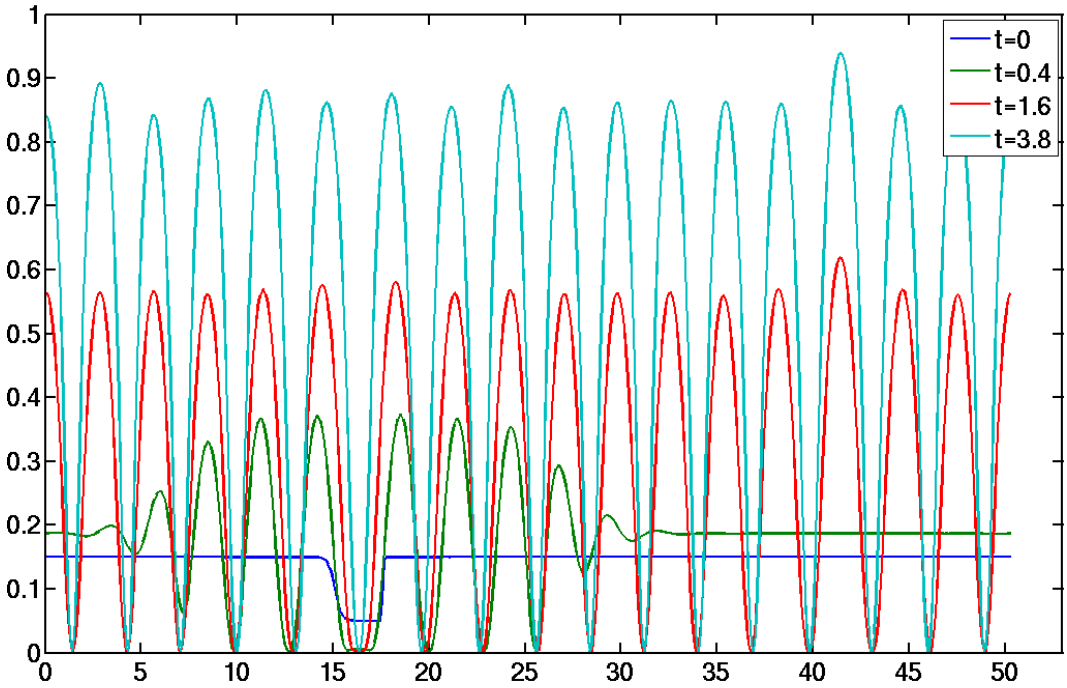

Figure 4.30: Evolution of regular array for $v_d = 0.1$, Υ_3 ($g = 0.0015, \beta = 16$), $h_f = 0.15, a = 0.125, N = 512$, $b = 2.5 \cdot 10^{-4}, r = 10^{-3}$.

Chapter 5

Discussion

Continuum model of thin film evolution used here allows to forget about the atomistic nature of growth phenomena, since the islands typically contain thousands of atoms and the continuum approximation is well satisfied. Quantum mechanical potentials, barriers etc. are not needed in the model and this is great advantage over the kinetic Monte Carlo models. In fact multiscale approaches are developed to use good properties of both models together. Our model is mostly independent of material properties and thus can be applied to any material system. The only parameters controlling the evolution are transition thickness wetting parameter b and the form of surface energy and its minima.

The smoothing property of the surface diffusion equation is propably the main disadvantage of the model, since it constrains evolution of the corners between facets and smoothes them. Here the atomic nature of the surface should be accounted for. Reduction of the full $2+1$ system (3D film with 2D surface) to the $1+1$ system can only describe experimentally observed elongated huts or ridges. Square pyramid islands reduce to triangles (with cut top) and important patterns of spatial organization are missed.

Isotropic linear elasticity is good approximation but large deformations could be present for large islands and this would require nonlinear elasticity. If different elastic constants are assumed, they will not substantially change the qualitative behavior, only the characteristic values of time and length. Elastic anisotropy is small normally and has no effect on our $1+1$ model but could produce interesting features in $2+1$ model.

Anisotropy of the surface energy is not well known and but it is a critical factor for evolution and stability of islands. Lower angles of minima produce islands with lower aspect ratio and thus smaller elastic relaxation. Different models appeared with one, two or more minima and their consequence the stability of islands was studied in literature. Surface energy in general depends on temperature, composition and other factors and needs to be studied experimentally and theoretically.

Discretizations errors can be disastrous if the grid resolution is too small. Otherwise the methods were very robust, but sometimes too slow. Finite size effect of periodic box is significant mainly for samples with one or very few is-

lands, where it can constrain the evolution mathematically. Larger samples are not influenced very much and can well approximate real experimental systems consisting of tens to hundreds of quantum dots.

Several directions could be possible to improve the numerical methods. Unstructured grid could be used with points redistributed by following the value of curvature. Admissible polygonal curves for surface height that would allow only certain tangent angles are possible (developed for crystalline curvature flow originally). Other stable time-stepping schemes which allow bigger timesteps at the prescribed relative tolerance would be also appreciated.

Three dimensional calculations would better describe the physical phenomena, but the extension of current method is not so straightforward. Hardest problem is the accurate computation of strain energy, because the complex formulation we introduced fails in 3D. Efforts were done to obtain expansion of strain energy to first and second order, but as the slope of the islands becomes large for real systems, these approximations are not enough. Coupled finite element calculation of strain energy and evolution of surface was beyond the scope of this work.

Summary

For a simple review on the main results of our simulations, see Table 5.1. Linear results are from the linear perturbation analysis, self-similar means that the surface pattern remains the same, but grows in amplitude. Metastable array suggests that the island are stable if not annealed for very long times. More comments can be found in appropriate results section. Analytical proof of the stability is not possible due to the great number of parameters.

Regime	isotropic Υ_1	smooth Υ_2	cusped Υ_3
linear, $b = 0, r = 0$	self-similar	self-similar	self-similar
nonlinear, $b = 0, r = 0$	cusps	cusps	cusps
nonlinear, $b \neq 0, r = 0$	ripening	numerically unstable	numerically unstable
nonlinear, $b \neq 0, r \neq 0$	ripening	faceted islands,ripening	faceted islands,ripening
nonlinear, $b \neq 0, r \neq 0$ $v_d = 0.1$	metastable array	metastable faceted array	metastable faceted array

Table 5.1: Review of the main results.

We have studied the evolution of quantum dots during heteroepitaxy of strained film on a substrate in two dimensions. Continuum model based on surface diffusion equation was formulated in nondimensional form. Chemical potential consisted of the strain energy, surface energy, wetting energy and corner regularization. Interaction of film and substrate was included with height-dependent surface energy, leading to the wetting energy term in the chemical potential, which prevented exposure of the substrate in the model. Anisotropic surface energy produced sharp corners at island edges and negative surface stiffness, causing numerical instability and ill-posedness of the evolution equation. To prevent these problems, corner regularization energy was added.

Elasticity problem for thin film was solved using Goursat functions by numerical quadrature on the boundary and analytically continued inside the film. Weak formulation for finite element method was derived but analytic results (existence, convergence) were seen miles away. Spectral methods were also presented and proved to be good choice for periodic boundary conditions. Resulting system of ODEs is very stiff and the numerical stability was obtained using stable A and $L-$stable method. Calculation of the stress tensor and dis-

placements inside the thin film was done numerically by analytic continuation.

We have compared the evolution for isotropic surface energy with known results. Wetting energy was seen to prevent the exposure of the substrate and leave thinner inter-island wetting layer between islands. In addition it stabilizes thin wetting layer below critical thickness as seen for Stranski-Krastanow growth. After the initial island formation, long time behavior reveals coarsening effect - vanishing of smaller islands at the expense of bigger.

Evolution for smoothly anisotropic surface energy leads to similar effects, but the islands are slightly faceted and grow with the same aspect ratio. After some critical width, they grow only vertically and pyramid-dome transition was qualitatively observed. These islands are metastable just for some time scale after formation. With the deposition from above, more regular island arrays were obtained and they were stable against coarsening. Main difference between 11° and 45° facet degrees lies in the lower aspect ratio of faceted islands and thus lower elastic relaxation. The shape transition occurs sooner and the corners are not so sharp for 11° facet.

Similar effects were seen for cusped surface energy, but the computations were very slow with the rounded version of surface stiffness (blow-ups at the maxima made the simulations untractable). Instead, stiffness without the blow-up was used and proved to give similar results as smooth surface energy. The only difference lies in the stability of facets, which can be greatly enhanced by the blow-up in surface stiffness.

List of symbols

Physical quantity	Nondimensional	Description
$\tilde{\gamma}$	γ	surface energy, per unit area
ε_0		misfit strain
E		Young modulus
ν		Poisson ratio
X, Y	x, y	cartesian coordinates
H	h	height of the film surface
T	t	time
Λ	λ	size of the periodic box
A	a	wavenumber of the periodic box
V_D	v_d	constant deposition rate
J_D	j_d	vertical deposition rate
a_s		lattice constant of the substrate
a_f		lattice constant of the film
$\tilde{\sigma}_{ij}$	σ_{ij}	stress tensor
ε_{ij}		strain tensor
N_X, N_Y	n_x, n_y	unit outer normal
$\tilde{S}$	S	strain energy density
V_N		velocity normal to the interface
V_{at}		atomic volume
J_S		surface diffusion flux
K	κ	curvature
$\tilde{\Upsilon}$	Υ	surface stiffness
$\tilde{\mu}_{surf}$	μ_{surf}	surface energy chemical potential
$\tilde{\mu}_{el}$	μ_{el}	elastic energy chemical potential
$\tilde{\mu}_{wet}$	μ_{wet}	wetting energy chemical potential
$\tilde{\mu}_{cor}$	μ_{cor}	corner energy chemical potential
$\tilde{\mu}$	μ	total chemical potential
H_f	h_f	initial film height
P_0	p_0	perturbation amplitude
B	b	transition wetting parameter
R	r	corner regularization parameter
	g	strength of surface anisotropy
	β	surface energy minima
	θ	tangent angle
	N	number of grid points

Bibliography

Bank, R. E., Coughran, Jr., W. M., Fichtner, W., Grosse, E. H., and Rose, D. J. 1985. Transient simulation of silicon devices and circuits. *IEEE Transactions on Electronic Devices* 32:1992–2007.

Bonzel, H. and Preuss, E. 1995. Morphology of periodic surface profiles below the roughening temperature: aspects of continuum theory. *Surface Science* 336:209–224.

Boyd, J. P. 2001. Chebyshev and Fourier Spectral Methods, 2nd Edition. Dover Publishers.

Chiu, C. H. and Gao, H. 1993. Stress singularities along a cycloid rough surface. *Int. J. Solids Struct.* 30:2983–3012.

Chiu, C.-H. and Gao, H. 1995. Numerical study of stress controlled surface diffusion during epitaxial film growth. *MATER RES SOC SYMP PROC.* 356:33–44.

Eisenberg, H. R. and Kandel, D. 2002. Origin and properties of the wetting layer and early evolution of epitaxially strained thin films. *Phys. Rev. B* 66:155429.

Eisenberg, H. R. and Kandel, D. 2005. Formation, ripening, and stability of epitaxially strained island arrays. *Phys. Rev. B* 71:115423.

Gill, S. P. A. private communication.

Kamins, T. I., Carr, E. C., Williams, R. S., and Rosner, S. J. 1997. Deposition of three-dimensional Ge islands on Si(001) by chemical vapor deposition at atmospheric and reduced pressures. *Journal of Applied Physics* 81:211–219.

Kukta, R. V. and Freund, L. B. 1997. Minimum energy configuration of epitaxial material clusters on a lattice-mismatched substrate. *Journal of the Mechanics and Physics of Solids* 45:1835–1860.

Long, F., Gill, S. P. A., and Cocks, A. C. F. 2001. Effect of surface-energy anisotropy on the kinetics of quantum dot formation. *Phys. Rev. B* 64:121307.

Medeiros-Ribeiro, G., Bratkovski, A. M., Kamins, T. I., Ohlberg, D. A. A., and Williams, R. S. 1998. Shape Transition of Germanium Nanocrystals on a Silicon(001) Surface from Pyramids to Domes. *Science* 279:353–355.

Mikhlin, S. G. 1957. Integral equations. Pergamon Press.

Mo, Y.-W., Savage, D. E., Swartzentruber, B. S., and Lagally, M. G. 1990. Kinetic pathway in stranski-krastanov growth of Ge on Si(001). *Phys. Rev. Lett.* 65:1020–1023.

Moison, J. M., Houzay, F., Barthe, F., Leprince, L., Andre, E., and Vatel, O. 1994. Self-organized growth of regular nanometer-scale InAs dots on GaAs. *Applied Physics Letters* 64:196–198.

Ozkan, C. S., Nix, W. D., and Gao, H. 1997. Strain relaxation and defect formation in heteroepitaxial SiGe films via surface roughening induced by controlled annealing experiments. *Applied Physics Letters* 70:2247–2249.

Pang, Y. and Huang, R. 2006. Nonlinear effect of stress and wetting on surface evolution of epitaxial thin films. *Phys. Rev. B* 74:075413.

Penev, E. S. 2002. On the theory of surface diffusion in InAs/GaAs(001) heteroepitaxy. PhD thesis, TU Berlin.

Rastelli, A., Kummer, M., and von Känel, H. 2001. Reversible shape evolution of Ge islands on Si(001). *Phys. Rev. Lett.* 87:256101.

Ross, F. M., Tersoff, J., and Tromp, R. M. 1998. Coarsening of self-assembled Ge quantum dots on Si(001). *Phys. Rev. Lett.* 80:984–987.

Siegel, M., Miksis, M. J., and Voorhees, P. W. 2004. Evolution of material voids for highly anisotropic surface energy. *Journal of the Mechanics and Physics of Solids* 52:1319–1353.

Spencer, B. J. 1999. Asymptotic derivation of the glued-wetting-layer model and contact-angle condition for stranski-krastanow islands. *Phys. Rev. B* 59:2011–2017.

Spencer, B. J. 2004. Asymptotic solutions for the equilibrium crystal shape with small corner energy regularization. *Physical Review E* 69:011603.

Spencer, B. J. and Meiron, D. I. 1994. Nonlinear evolution of the stress-driven morphological instability in a two-dimensional semi-infinite solid. *Acta metall. mater.* 42:3629–3641.

Spencer, B. J. and Tersoff, J. 2001. Stresses and first-order dislocation energetics in equilibrium stranski-krastanow islands. *Phys. Rev. B* 63:205424.

Spencer, B. J., Voorhees, P. W., and Tersoff, J. 2001. Morphological instability theory for strained alloy film growth: The effect of compositional stresses and species-dependent surface mobilities on ripple formation during epitaxial film deposition. *Phys. Rev. B* 64:235318.

Srolovitz, D. J. 1989. On the stability of surfaces of stressed solids. *Acta metall.* 37:621–625.

Stangl, J., Holy, V., and Bauer, G. 2004. Structural properties of self-organized semiconductor nanostructures. *Reviews of Modern Physics* 76:725.

Tekalign, W. T. and Spencer, B. J. 2004. Evolution equation for a thin epitaxial film on a deformable substrate. *Journal of Applied Physics* 96:5505–5512.

Tersoff, J., Spencer, B. J., Rastelli, A., and von Känel, H. 2002. Barrierless formation and faceting of SiGe islands on Si(001). *Phys. Rev. Lett.* 89:196104.

Tromp, R. M., Ross, F. M., and Reuter, M. C. 2000. Instability-driven SiGe island growth. *Phys. Rev. Lett.* 84:4641–4644.

Weideman, J. A. and Reddy, S. C. 2000. A matlab differentiation matrix suite. *ACM Trans. Math. Softw.* 26:465–519.

Yang, W. H. and Srolovitz, D. J. 1993. Cracklike surface instabilities in stressed solids. *Phys. Rev. Lett.* 71:1593–1596.